Regime maps for sloshing in horizontal cylindrical tanks under vertical acceleration

Francisco Monteiro,[1,2,*] Tommaso De Maria,[1,3] Samuel Ahizi,[1,2] Ramon Abarca,[4]
Giuseppe C. A. Caridi,[1] and Miguel A. Mendez[1,2,5]
[1] *von Karman Institute for Fluid Dynamics, Waterloosesteenweg 72, Sint-Genesius-Rode, Belgium*
[2] *Aerospace Engineering Research Group, Universidad Carlos III de Madrid, Leganés, 28911 Madrid, Spain*
[3] *SAAS, Université Libre de Bruxelles, Brussels, Belgium*
[4] *Airbus Operations S.L., 28906 Getafe, Spain*
[5] *Aero-Thermo-Mechanics Laboratory, École Polytechnique de Bruxelles, Université Libre de Bruxelles, Brussels, Belgium*

(Received 2 December 2025; accepted 4 August 2026; published 28 August 2026)

Vertical excitation of partially filled horizontal cylindrical tanks can induce large-amplitude sloshing, particularly when the forcing frequency approaches twice the fundamental sloshing frequency, leading to parametric resonance. Under these conditions, parametric resonance can trigger exponential growth of free-surface perturbations, leading to large-amplitude waves, interface breakup, and enhanced mixing. In this work, we experimentally investigate the sloshing regimes associated with this primary parametric instability. Experiments are conducted in a transparent horizontal cylindrical tank ($D = 134.5\,\mathrm{mm}$, $L = 336.3\,\mathrm{mm}$) over a range of fill ratios and excitation conditions. A data-driven, image-based methodology is developed to identify and classify sloshing regimes directly from high-speed visualizations. The approach combines multiscale proper orthogonal decomposition for feature extraction with prototype-based clustering and support vector machine classification. The results are summarized in a dimensionless regime map across three fill ratios ($H_l/D \in [0.40; 0.67]$), distinguishing stable free-surface conditions, dominant longitudinal modes, and mixed or mode-interaction regimes. The map provides a structured characterization of the flow responses in the vicinity of the primary parametric resonance.

DOI: 10.1103/t48x-53br

I. INTRODUCTION

Sloshing is a major concern in engineering systems that store large fluid volumes, including chemical and power plants, aircraft and rocket propellant tanks, and marine vessels [1,2]. Induced by seismic forcing or vehicle accelerations, sloshing generates dynamic loads that can affect stability, maneuverability, and structural integrity [3,4]. Predicting and mitigating these effects requires an accurate characterization of the flow dynamics, which depend primarily on tank geometry, excitation direction, and fill level [5–8].

Most studies have focused on upright cylindrical tanks subjected to lateral excitation, a configuration of particular importance in early space programs, where sloshing played a key role during ascent [9–12]. This body of work led to the development of dimensionless forcing diagrams characterizing the flow regimes near the fundamental sloshing mode [13], where swirling and chaotic motions may arise depending on the ratio between forcing and natural frequencies [14,15].

[*] Contact author: francisco.monteiro@vki.ac.be

Sloshing induced by vertical acceleration in horizontal cylindrical tanks has received comparatively limited attention, although this configuration is gaining renewed relevance in hydrogen-powered aviation, where cryogenic fuel storage may be distributed within the airframe and subjected to low-frequency, quasi-harmonic vertical excitations induced by turbulence, gusts, or control inputs. This renewed interest is reflected in recent efforts such as the SLOWD [16–20] and HASTA [21] projects. In this setting, parametric resonance may arise when the forcing frequency ω_f approaches twice the natural frequency of a sloshing mode, $\omega_{m,n}$, leading to subharmonic free-surface instabilities [22–24]. Here, m and n denote the longitudinal (number of half-wavelengths along the tank axis) and transverse (number of nodal diameters in the cross-section) mode indices, respectively.

In vertically forced sloshing, excitation modulates the effective gravity, the restoring force for free-surface oscillations in laterally excited systems. Although this requires larger forcing amplitudes than lateral excitation [25,26] to initiate sloshing, the resulting parametric resonance can produce much stronger amplification of free-surface disturbances [27,28].

The onset of parametric waves is classically described by the Mathieu equation, whose instability regions are represented in Ince-Strutt diagrams around subharmonic and harmonic frequencies [29,30]. In practice, the most critical responses are associated with the lowest-frequency modes, for which viscous damping is relatively weak [31]. Within the instability regions, free-surface perturbations can undergo exponential growth and evolve toward finite-amplitude wave states, with mode competition arising from overlapping instability bands [25,32]. Outside these regions, the free surface remains stable, aside from a weak response at the forcing frequency [33–35].

Most experimental studies of sloshing near parametric resonance have focused on high-aspect-ratio rectangular tanks ($L/D \gg 1$), where longitudinal modes dominate and transverse motion is suppressed [36–38]. In this configuration, attention has primarily been given to the second ($m = 2, n = 0$) and third ($m = 3, n = 0$) longitudinal modes, including phenomena such as jet formation at wave crests, and to classifications of Faraday waves as regular, irregular, or breaking [8,39]. In most cases, however, these classifications rely on visual inspection at each operating condition.

Beyond rectangular tanks, studies in cylindrical and square geometries have reported a wider range of dynamics, including single-mode responses, mode competition with periodic or chaotic transitions, and rotational states arising from degenerate or interacting modes [40–44].

For horizontal cylindrical tanks, prior work has primarily focused on lateral and pitching excitations [2,45–47] or on the numerical estimation of natural frequencies [48,49]. More recently, quasi-two-dimensional configurations ($L \ll D$) have been investigated to isolate transverse dynamics, restricting the response to modes with $m = 0$ [50–52].

Sloshing under vertical excitation in horizontal cylindrical tanks, particularly near parametric resonance, remains insufficiently characterized from an applied perspective. Although the onset of instability can be described theoretically, the resulting nonlinear dynamics and regime transitions are not organized into predictive frameworks, and no experimentally grounded regime map is currently available for this configuration. The present study provides an experimental characterization of sloshing in a horizontal cylindrical tank subjected to vertical excitation near the primary parametric resonance $\omega_f \approx 2\,\omega_{1,0}$. The analysis focuses on the $(m, n) = (1, 0)$ mode, corresponding to the first longitudinal mode with a nodal line at mid-length and no transverse variation. High-speed backlight visualizations are used to capture the free-surface dynamics, which are analyzed through multiscale modal decomposition. The resulting data are then used to construct a regime map by grouping responses with similar dynamical signatures using a data-driven clustering approach. While modal and wavelet-based analyses have previously been applied to sloshing [53,54], and prototype-based methods are well established in image analysis [55–57], their combination here provides a systematic framework to identify and organize the dominant sloshing regimes in relation to the underlying parametric-instability structure.

The article is organized as follows. Section II presents the problem and quantities of interest. Section III introduces the Mathieu equation and defines the onset conditions of instability regions relevant to parametrically excited sloshing. Section IV describes the experimental setup.

Section V details the methodology, including image processing, a clustering algorithm, and an automatic classification tool for identifying the sloshing regime. Section VI presents the experimental results, including natural frequency estimation, viscous damping factor computation, and neutral-stability boundary maps for multiple fill levels. Section VII concludes with final remarks and perspectives.

II. INVESTIGATED CONDITIONS

The configuration of interest is a horizontal cylindrical tank of radius R and length L, closed by spherical domes of radius R_d. The centers of the domes lie a distance l_d from the flat cylinder-dome interface. The tank is filled to height H_l (from the bottom) with a liquid of density ρ and dynamic viscosity μ. The remaining ullage contains air, whose properties are neglected in the sloshing analysis. The gas-liquid surface tension is σ.

The tank undergoes vertical harmonic motion $z(t) = A_f \sin(\omega_f t)$, with forcing amplitude A_f and angular frequency ω_f. The effective vertical acceleration is $a_z(t) = -g - A_f\omega_f^2 \sin(\omega_f t)$, where $g = 9.81\ \mathrm{m\,s^{-2}}$ is gravitational acceleration.

Denoting the interface dynamics by $\eta(\boldsymbol{x}, t)$, where $\boldsymbol{x} = (x, y) \in \mathbb{R}^2$ represents the in-plane (horizontal) coordinate vector, the problem depends on three geometrical parameters, one kinematic parameter, one operational parameter (the liquid fill level), and three dimensionless numbers governing the force balance:

$$\frac{\eta(\boldsymbol{x}, t)}{R} = f\left(\frac{L}{R}, \frac{R_d}{R}, \frac{l_d}{R}, \frac{A_f}{R}, \frac{H_l}{D}, \mathrm{Re}, \mathrm{Fr}, \mathrm{We}\right), \tag{1}$$

where $\mathrm{Re} = \rho[U]R/\mu$ is the Reynolds number, $\mathrm{We} = \rho[U]^2R/\sigma$ is the Weber number and $\mathrm{Fr} = [U]/\sqrt{gR}$ is the Froude number. Here, the reference velocity is taken as $[U] = (A_f\, \omega_f)$. Within the range of investigated conditions, surface tension and wetting effects can be considered negligible, since We ranges from $\mathcal{O}(10^1)$ to $\mathcal{O}(10^3)$ and the ratio $\mathrm{Bo} = \mathrm{We}/\mathrm{Fr}^2$, known as Bond number [58], is of $\sim\mathcal{O}(10^3)$. The Reynolds number lies between $\mathcal{O}(10^3)$ and $\mathcal{O}(10^4)$, and thus moderate turbulence is to be expected, while the Froude number remains below unity in all experiments; hence the investigated conditions are clearly in gravity-dominated conditions [1,4].

Sloshing regimes are usually analyzed in terms of the system's natural frequency. For vertical excitation, one considers the ratio $\omega_f/(2\,\omega_{1,0})$, which scales the forcing frequency by the first longitudinal mode because the first parametric resonance occurs near $\omega_f \approx 2\,\omega_{1,0}$. Analytical expressions for these natural frequencies exist only for flat-end cylindrical tanks [48], not for the dome-ended geometries studied here. Thus, $\omega_{1,0}$ was obtained experimentally from free-decay tests (Sec. V A). The resulting frequencies (Sec. VI A) are much lower than those predicted by the flat-end cylinder model of Hasheminejad and Soleimani [48], listed in the Appendix.

The experimental campaign was conducted at three fill ratios, $H_l/D = 0.40, 0.50$, and 0.67. Table I summarizes the range of conditions ($A_f\omega_f^2/g$, A_f/R, $\omega_f/(2\,\omega_{1,0})$) and the number of tests, N_{pts}, for each fill level. Within these ranges, sampling followed a two-stage approach. First, amplitude sweeps at a constant forcing frequency near the primary resonance, $\omega_f/(2\,\omega_{1,0}) \approx 1$, were performed to determine the critical amplitude at the transition between stable and unstable dynamics. Second, we carried out a randomized, space-filling exploration of the remaining domain to achieve extensive coverage.

III. PARAMETRIC RESONANCE AND INSTABILITY REGIONS

Vertical acceleration induces a time-periodic modulation of the effective gravity acting on the liquid. Within the classical linear potential-flow framework, with linearized free-surface boundary conditions [1], the interface elevation can be decomposed into modes, each of which satisfies a parametrically forced oscillator equation of Mathieu type (see, e.g., Refs. [6,24,25,29]). Accordingly, each mode (m, n) is characterized by its natural frequency $\omega_{m,n}$ and damping ratio $\zeta_{m,n}$, and

TABLE I. Experimental matrix summarizing the investigated conditions. Reported parameters include the liquid fill ratio H_l/D, the number of test points N_{pts}, and the estimated natural frequency $\bar{\omega}_{1,0}$ and damping ratio $\bar{\zeta}_{1,0}$ of the $(1,0)$ mode (sample means with 95% confidence intervals). Excitation conditions are given in terms of the dimensionless vertical acceleration $A_f\omega_f^2/g$, displacement amplitude A_f/R, and normalized forcing frequency $\omega_f/(2\,\omega_{1,0})$.

H_l/D	N_{pts}	$\bar{\omega}_{1,0}$ [rad s^{-1}] (95% CI; $N=4$)	$\bar{\zeta}_{1,0}$ [$-$] (95% CI; $N=4$)	$A_f\omega_f^2/g$ [$-$]	A_f/R [$-$]	$\omega_f/(2\,\bar{\omega}_{1,0})$ [$-$]
0.67	66	7.12 ± 0.03	0.015 ± 0.002	$0.02 - 0.94$	$0.02 - 0.58$	$0.90 - 1.20$
0.50	73	6.08 ± 0.16	0.004 ± 0.001	$0.02 - 0.77$	$0.02 - 0.62$	$0.90 - 1.20$
0.40	61	5.32 ± 0.02	0.006 ± 0.002	$0.02 - 0.48$	$0.02 - 0.52$	$0.87 - 1.16$

its modal amplitude $\eta_{m,n}(t)$ satisfies

$$\frac{d^2\eta_{m,n}(t)}{dt^2} + 2\,\zeta_{m,n}\,\omega_{m,n}\,\frac{d\eta_{m,n}(t)}{dt} + \omega_{m,n}^2\left(1 - \frac{A_f\,\omega_f^2}{g}\cos(\omega_f t)\right)\eta_{m,n}(t) = 0. \tag{2}$$

Although the tank motion is applied as a sinusoidal displacement $z(t) = A_f \sin(\omega_f t)$ (see Sec. II), the cosine form is adopted here for consistency with the canonical Mathieu equation [59,60], noting that a phase shift of $\pi/2$ does not affect the predicted stability boundaries.

The instability regions of (2), discussed in Sec. VI E, are computed using Floquet stability theory, following the formulation summarized by Ibrahim [6]. The equation is recast as a first-order system with periodic coefficients and integrated over one forcing period $T = 2\pi/\omega_f$ to construct the monodromy matrix mapping the system state from t to $t+T$. The Floquet multipliers, defined as the eigenvalues of this matrix, determine stability: the boundary of each instability region corresponds to parameter combinations $(A_f/R,\ \omega_f/(2\,\omega_{m,n}))$ for which at least one multiplier lies on the unit circle, marking the transition from bounded to exponentially growing solutions.

The resulting neutral-stability boundaries define the so-called Mathieu tongues, which arise near subharmonic orders of the natural frequency, $\omega_f \approx 2\,\omega_{m,n}/r$ with $r = 1, 2, 3, \ldots$. The principal instability region ($r=1$) corresponds to the classical Faraday subharmonic resonance [22]. Additional details on the structure of these instability regions in horizontal cylindrical tanks are discussed by Ahizi [61].

It is worth noting that (2) includes viscous dissipation through the linear damping term $2\,\zeta_{m,n}\,\omega_{m,n}$, which is absent in the inviscid formulation of Benjamin and Ursell [29]. This extension, introduced by Brand and Nyborg [26], accounts for the experimentally observed shift in instability thresholds: while the inviscid model predicts instability at arbitrarily small forcing amplitudes, the inclusion of damping leads to a finite critical threshold ($A_f/R > 0$ at $\omega_f/(2\,\omega_{1,0}) = 1$).

In this work, we focus on the principal parametric-instability region associated with the $(m,n) = (1,0)$ mode. As this mode has the lowest natural frequency, it defines the first and widest accessible instability domain. Equation (2) is used as a reduced-order framework to guide the interpretation of the experimentally observed sloshing regimes and to support the data-driven classification introduced in Sec. V D.

IV. EXPERIMENTAL SETUP

The experimental setup, shown in Fig. 1, consists of a transparent polymethyl methacrylate (PMMA) reservoir with circular cross-section with diameter $D = 134.5$ mm, length $L = 336.3$ mm, and aspect ratio $L/R = 5.0$. Each end of the tank is closed by a spherical dome of radius $R_d = 100.0$ mm and depth 25.0 mm, whose center of curvature lies $l_d = 75.0$ mm inside the cylindrical section of the tank.

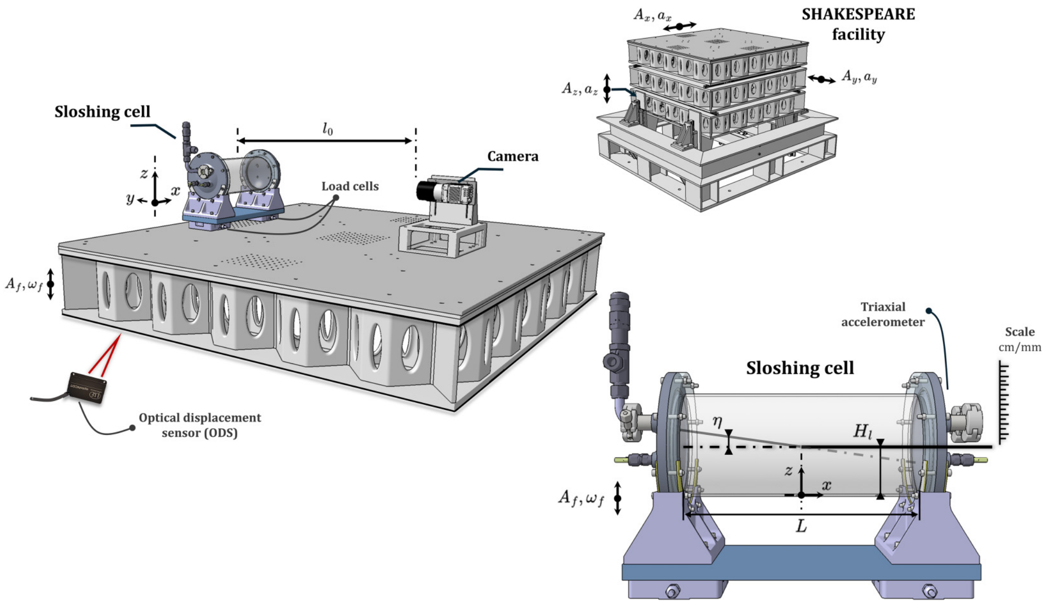

FIG. 1. Experimental setup integrated in the three-axis SHAKESPEARE sloshing table facility. The sloshing cell consists of a horizontal cylindrical PMMA test section with radius R and length L (aspect ratio $L/R = 5.0$), closed by aluminum domed end caps. A high-speed camera records the free-surface displacement $\eta(t)$ at the fill level H_l under imposed vertical excitation characterized by amplitude $A_z \equiv A_f$ and angular frequency $\omega_z \equiv \omega_f$, producing an effective vertical acceleration $a_z(t) = -g - A_f\omega_f^2 \sin(\omega_f t)$. The dynamic conditions are monitored using an optical displacement sensor (ODS) and a triaxial accelerometer.

The cell was partially filled with demineralized water, and air at ambient pressure occupied the ullage space. Tests were performed under near-isothermal conditions, with ambient temperature in the range $T_{\mathrm{amb}} = [290,\ 298]$ K. Within the range of temperatures in the experiments, the average liquid properties, as computed from REFPROP [62], are $\rho = 998\,\mathrm{kg\,m^{-3}}$, $\mu = 981\,\mu\mathrm{Pa\,s}$, and $\sigma = 72.6\,\mathrm{mN\,m^{-1}}$.

Optical measurements using backlighting were performed with a JAI SP-12000MCXP4 high-speed camera at 70 Hz equipped with a $f = 75$ mm objective lens. The focal ratio was fixed at $f/4.0$. The camera was mounted on the sloshing table at a distance of $l_0 = 375$ mm, supported by a rigid, adjustable mount that enabled fine vertical positioning. Yaw and pitch were minimized to maintain normal alignment with the test cell. Fill-level measurements were tracked using two reference methods: an external scale visible in the camera's field of view and an immersed probe used before each test. The fill level measurement uncertainty is estimated to be $\delta H_l = \pm 5.0$ mm.

The sloshing cell was mounted on aluminum feet via flanges attached to its end domes and securely bolted to a base plate (see bottom of Fig. 1). This base plate was connected to two three-axis load cells (ME K3D120, ± 1000 N) for force measurements. The load cells were, in turn, coupled to a stainless steel fastening plate (excluded from Fig. 1), which was mounted on the SHAKESPEARE sloshing table. This three-axis table enables controlled harmonic excitations along each axis, prescribed by amplitudes A_x, A_y, and A_z, and angular frequencies ω_x, ω_y, and ω_z, with $A_z \equiv A_f$ and $\omega_z \equiv \omega_f$ for the vertical direction, with amplitudes up to $A_f = \pm 45$ mm, forcing frequencies in the range $\omega_f \in [0, 63]\,\mathrm{rad\,s^{-1}}$ or $f_f \in [0, 10]$ Hz, and accelerations reaching up to $A_f\omega_f^2/g \in [0, 1]$. Dynamic conditions are tracked through a triaxial accelerometer (Endevco Model 7298-2) with the uncertainty identified to be $\delta a/g = \pm 0.01$, and an optical displacement sensor (ODS) (Optoepsilon optoNCDT ILD1302-100) with $\delta A = \pm 0.5$ mm.

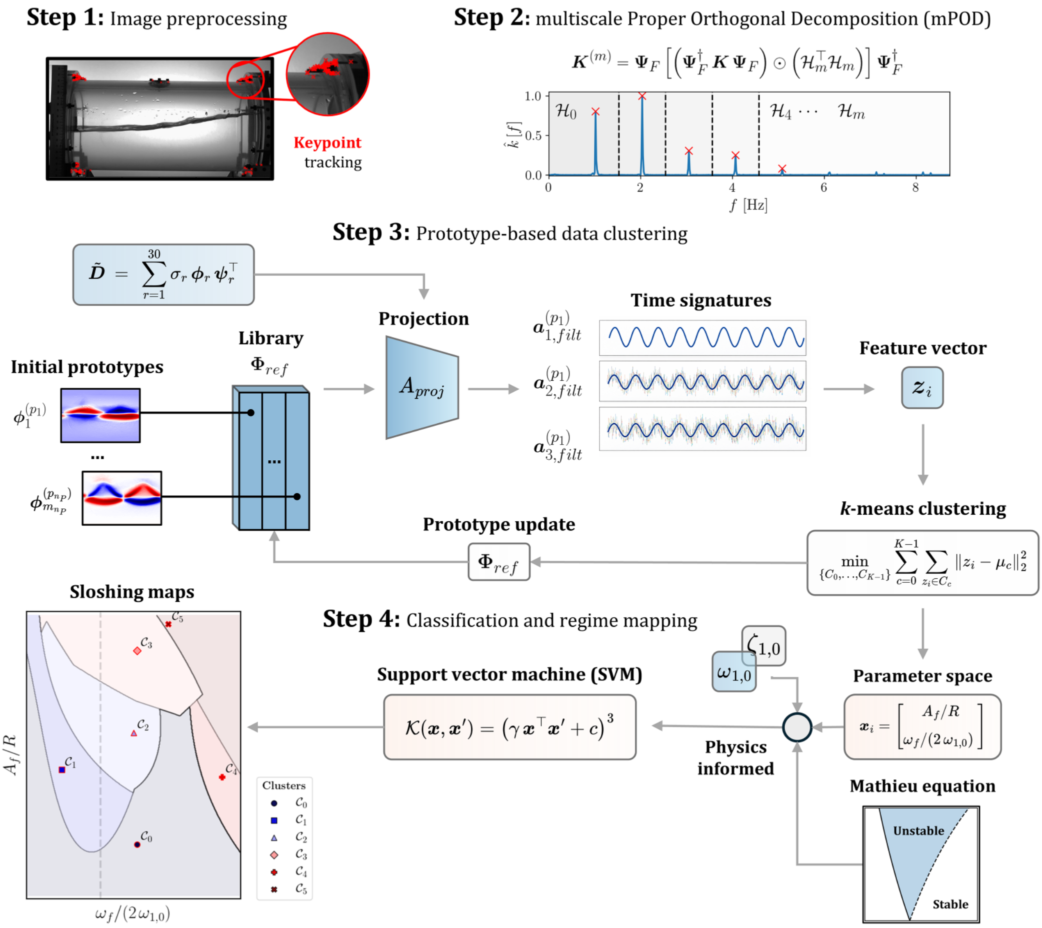

FIG. 2. Flowchart of the proposed algorithm. Step 1: acquired image sequences are pre-processed to correct for unwanted vibrations. Step 2: the mPOD is used to analyze the acquired snapshots between $t \in [0, 60]$ seconds. Data is then truncated to the first $n_R = 30$ mPOD modes. Step 3: an initial reference prototype library ($\mathbf{\Phi}_{\text{ref}}$) is defined from representative free-surface behaviors, and each truncated test case ($\tilde{\boldsymbol{D}}$) is projected onto it to obtain projected temporal signatures and feature vectors ($\boldsymbol{A}_{\text{proj}} \to z_i$). Finally, unsupervised k-means clustering is used to label the data, and a nonlinear multiclass SVM determines continuous decision boundaries between sloshing regimes (Step 4).

V. DATA-DRIVEN IDENTIFICATION AND CLASSIFICATION OF SLOSHING REGIMES

This section presents the data-driven, image-based methodology developed to identify and classify sloshing regimes. An overview of the complete workflow is shown in Fig. 2, which is organized into four main steps.

Step 1: Image preprocessing. Raw high-speed image sequences are stabilized and corrected to remove camera vibrations, small frame rotations, and nonuniform illumination. Keypoints are tracked between consecutive frames using the oriented-fast and rotated-brief (ORB) detector, and affine transformations are applied to align the sequence with a fixed reference frame. Residual tilt is corrected through Hough-line detection, while global intensity variations are compensated by histogram equalization and local mean subtraction. These operations, implemented with standard OpenCV routines [63], ensure that only the fluid motion contributes to the subsequent analysis.

Step 2: Multiscale modal decomposition. The stabilized image sequences are analyzed with multiscale proper orthogonal decomposition (mPOD), applied directly to the video frames. This yields a compact representation by separating the signal into a few modes, each tied to a specific frequency band. Dominant sloshing motions—such as subharmonic oscillations near parametric resonance—are thus isolated from higher-frequency content and noise. The resulting modal coefficients describe the temporal evolution and relative strength of the main flow components.

Step 3: Prototype-based data clustering. For each fill level, representative reference cases are first selected by inspecting the experimental responses and their modal content, to initialize a prototype library spanning the main sloshing behaviors. Each test case is then projected onto this basis to obtain energy-based feature vectors that quantify the activation of each prototype mode, i.e., its similarity to the reference free-surface responses. These vectors are then clustered using the k-means algorithm, so that regime labels emerge from grouping cases with similar energy signatures. The prototypes are iteratively updated using the cluster medoids until convergence, reducing sensitivity to the initial selection. In this way, the prototypes provide a physics-guided representation of the dominant sloshing behaviors, while the regime labels are determined by the clustering.

Step 4: Classification and regime mapping. A nonlinear support vector machine (SVM) with a polynomial kernel (Sec. V D) is trained on the clustered data to delineate regime boundaries in the nondimensional parameter space $(A_f/R,\ \omega_f/(2\,\omega_{1,0}))$. The classifier is informed by the Mathieu-equation stability analysis (Sec. III), linking experimental observations to the theoretical instability regions.

A. Experimental protocol and identification of natural frequency and damping ratio

In the absence of forcing, Eq. (2) reduces the time evolution of each mode to that of a second-order damped oscillator [1,6]. Accordingly, the natural frequency of the antisymmetric longitudinal mode $(m, n) = (1, 0)$, $\omega_{1,0}$, and its associated damping ratio, $\zeta_{1,0}$, were identified from free-decay tests. Alternative approaches are discussed by Casiano [64].

The experimental protocol was designed to ensure that the sloshing response reached a fully developed state prior to analysis. In particular, the procedure consisted of first forcing the system near the expected (1,0) parametric-resonance to trigger a response dominated by the first antisymmetric longitudinal mode. For this initial phase, the forcing frequency was set to the theoretical value predicted by potential-flow analysis for a flat-ended cylindrical tank [48]. This estimate was used only to position the excitation near the target mode. The resonance condition was then refined experimentally until a fully developed periodic response was obtained; the excitation was then stopped, and the ensuing free decay was recorded. The forcing duration was fixed to 60 s, which was sufficient for the experimentally observed response to reach its developed regime across all investigated test cases. Throughout all experiments, the identification procedure relied on synchronized high-speed imaging and load-cell measurements providing the vertical forces $F_{z_1}(t)$ and $F_{z_2}(t)$ at the tank supports, together with the platform acceleration signal $a_z(t)$. These measurements were used to monitor the time evolution of the free-surface and to assess the consistency of the hydrodynamic response.

Conventional image-based tracking of the free surface (e.g., Refs. [7,12,65]) was not applicable across the present dataset, due to interface breakup, droplet ejection, and fragmentation, which prevent robust and consistent interface reconstruction. The high-speed image sequences were therefore analyzed using the mPOD approach. Balancing energy optimality and frequency selectivity, the temporal structure of the leading mPOD mode $\boldsymbol{\psi}_1$ [see Eq. (8)] accurately captures the dominant sloshing dynamics, while its associated spatial mode $\boldsymbol{\phi}_1$ confirms that the identified response corresponds to the expected $(m, n) = (1, 0)$ antisymmetric mode.

The time series of all measured quantities—$\psi_1(t)$, $F_{z_1}(t)$, $F_{z_2}(t)$, and $a_z(t)$—were analyzed using a continuous wavelet transform (CWT) to resolve the time-dependent evolution of their spectral content. A complex Morlet wavelet was selected because the analyzed signals are predominantly oscillatory and narrowband, with transient variations in amplitude and frequency, particularly during the transition from forced oscillations to free decay. Under these conditions, the Morlet wavelet provides a suitable compromise between temporal and spectral resolution, and has likewise been adopted in related studies addressing similar identification tasks [53,61,66]. The wavelet was implemented with a bandwidth parameter of 6.0, a center frequency of 2.0, and 64 voices per octave.

The instantaneous dominant frequency is extracted as

$$f_r(t) = \arg\max_{f \in \mathcal{B}} P(t, f), \tag{3}$$

where $P(t, f)$ denotes the wavelet power, defined as the squared magnitude of the complex CWT coefficients. The frequency domain $\mathcal{B}$ is determined by the sampling frequency and the chosen wavelet parameters, and in this analysis, it was restricted to the band encompassing the fundamental sloshing mode. This approach provides a smooth estimate of the temporal evolution of the resonance frequency during the transition from the forced to the free-decay regime.

Once the external excitation is stopped, the dominant frequency $f_r(t)$ transitions from the forcing frequency toward the damped natural frequency of the (1,0) mode (see Sec. VI A). This behavior is clearly observed in the CWT ridge of the image-derived signal $\psi_1(t)$ and in the load-cell forces $F_{z_1}(t)$ and $F_{z_2}(t)$, whereas the accelerometer signal $a_z(t)$ primarily reflects the imposed platform motion and therefore captures only the pre-ring-down stage.

The ring-down interval $t \in [t_1, t_2]$ is defined as a portion of the signal following the cessation of forcing. The initial time t_1 is selected when the subharmonic ridge power, $P_r(t) = |W(t, f_r(t))|^2$, first exceeds the residual power associated with the forcing component in F_{z_1} and F_{z_2}. Within this window, the liquid oscillates freely at the damped natural frequency,

$$\omega_{d_{1,0}} = \omega_{1,0}\sqrt{1 - \zeta_{1,0}^2}, \quad f_{1,0} = \frac{\omega_{1,0}}{2\pi}, \tag{4}$$

which is estimated directly from the ridge as

$$f_{d_{1,0}} = \operatorname*{median}_{t \in [t_1, t_2]} f_r(t), \quad \omega_{d_{1,0}} = 2\pi f_{d_{1,0}}, \tag{5}$$

where the median acts as a robust estimator against local fluctuations. The damping ratio is obtained from the temporal decay of the ridge power within the same interval. Because the CWT ridge behaves as a time-localized band-pass filter centered on the mode of interest, the ridge power decays approximately exponentially as $P_r(t) \propto e^{-2\,\zeta_{m,n}\,\omega_{m,n}\,t}$ for a correctly isolated second-order response [67,68]. Taking the logarithm gives

$$\ln P_r(t) = -2\,\zeta_{m,n}\,\omega_{m,n}\,t + \ln P_0, \tag{6}$$

so that the slope of a first-order least-squares fit of $\ln P_r(t)$ versus t over $[t_1, t_2]$ yields the mean damping ratio $\zeta_{m,n}$. The resulting values of $\omega_{1,0}$ and $\zeta_{1,0}$ serve as inputs for the Floquet analysis and are subsequently used to normalize the excitation parameters in the sloshing-regime maps of Sec. VI E.

B. Regime prototype definition via mPOD

The mPOD [69–71] is a data-driven modal decomposition that constrains the energy optimality of the proper orthogonal decomposition (POD) with a filter bank that allows for the spectral separation of its modes. This combination isolates nearly harmonic dynamics undergoing transient evolution and it is thus well suited to the narrow-band yet nonstationary nature of sloshing responses. The mPOD of the video sequence provides a reduced-order space to encode the sloshing response from the high-speed videos (Step 2; see Fig. 2).

As in all data-driven decompositions, the grayscale image sequence acquired during the experiments is arranged into the snapshot matrix $\boldsymbol{D} \in \mathbb{R}^{n_s \times n_t}$, whose columns correspond to vectorized frames:

$$\boldsymbol{D} = \begin{bmatrix} g_1[1,1] & \cdots & g_{n_t}[1,1] \\ \vdots & \ddots & \vdots \\ g_1[n_x,1] & \cdots & g_{n_t}[n_x,1] \\ g_1[1,2] & \cdots & g_{n_t}[1,2] \\ \vdots & \ddots & \vdots \\ g_1[n_x,n_z] & \cdots & g_{n_t}[n_x,n_z] \end{bmatrix} \in \mathbb{R}^{n_s \times n_t}, \tag{7}$$

where each image $g_k[i, j] \in [0, 255]$ has spatial dimensions $n_s = n_x \times n_z$ and n_t denotes the total number of frames. As in classical POD, the mPOD represents the data as

$$\boldsymbol{D} = \sum_{r=1}^{n_R} \sigma_r \, \boldsymbol{\phi}_r \, \boldsymbol{\psi}_r^\top = \boldsymbol{\Phi} \, \boldsymbol{\Sigma} \, \boldsymbol{\Psi}^\top, \tag{8}$$

where $\boldsymbol{\phi}_r$ and $\boldsymbol{\psi}_r$ are the spatial and temporal modes, and σ_r is the associated amplitude.

In contrast with the classical POD, whose temporal modes are the eigenvectors of the correlation matrix $\boldsymbol{K} = \boldsymbol{D}^\top \boldsymbol{D}$ and may exhibit broad spectral content, the mPOD introduces a multiresolution analysis of $\boldsymbol{K}$. The correlation matrix is decomposed into band-limited components associated with n_M nonoverlapping frequency bands,

$$\boldsymbol{K} \approx \sum_{m=0}^{n_M - 1} \boldsymbol{K}^{(m)}, \tag{9}$$

each obtained by filtering $\boldsymbol{K}$ in the frequency domain as

$$\boldsymbol{K}^{(m)} = \boldsymbol{\Psi}_F [(\boldsymbol{\Psi}_F^\dagger \boldsymbol{K} \boldsymbol{\Psi}_F) \odot (\mathcal{H}_m^\dagger \mathcal{H}_m)] \boldsymbol{\Psi}_F^\dagger, \tag{10}$$

where $\boldsymbol{\Psi}_F \in \mathbb{C}^{n_t \times n_t}$ is the discrete Fourier transform matrix, $\mathcal{H}_m \in \mathbb{C}^{1 \times n_t}$ collects the discrete transfer function of the m-th band-pass filter, and $\odot$ denotes the Hadamard product. The product $\mathcal{H}_m^\dagger \mathcal{H}_m$ ensures that $\boldsymbol{K}^{(m)}$ remains Hermitian and thus has real, orthogonal eigenvectors. Ensuring that the filter bank satisfies a partition of unity,

$$\sum_{m=0}^{n_M - 1} \mathcal{H}_m = \mathbf{1}, \quad \mathcal{H}_m \odot \mathcal{H}_{m'} = \mathbf{0} \quad (m \neq m'), \tag{11}$$

the spectral bands are nonoverlapping and complete, guaranteeing that the temporal modes obtained from the eigenproblem

$$\boldsymbol{K}^{(m)} \, \boldsymbol{\psi}^{(m)} = \lambda^{(m)} \, \boldsymbol{\psi}^{(m)} \tag{12}$$

are mutually orthogonal across scales. Aggregating the eigenvectors of all bands yields the full mPOD temporal basis $\boldsymbol{\Psi}$, which remains orthogonal while offering controlled spectral separation among its modes.

Once the temporal structures are computed, the spatial structures and modal amplitudes are recovered through temporal projection, following the classical snapshot-based POD framework [72]:

$$\boldsymbol{\Phi} = \boldsymbol{D} \, \boldsymbol{\Psi} \, \boldsymbol{\Sigma}^{-1}, \quad \sigma_r = \|\boldsymbol{D} \, \boldsymbol{\psi}_r\|_2. \tag{13}$$

A consequence of the spectral separation achieved by mPOD is that the resulting spatial structures are no longer strictly orthogonal, in contrast to those obtained via standard POD. Nevertheless, the method yields modes that are energetically optimal within each spectral band and temporally well localized, enabling a clear association between individual modes and specific sloshing frequencies. In this study, the leading temporal coefficient $\boldsymbol{\psi}_1$ captures the time-resolved evolution of the dominant sloshing mode, while the reduced modal space spanned by the leading mPOD modes provides a compact and physically interpretable representation in which distinct sloshing regimes can be clearly separated despite the transient dynamics.

C. Data labeling and clustering

The proposed data-labeling and clustering strategy follows a prototype-based, semi-supervised approach to group experimental realizations (videos) that exhibit similar flow dynamics or regime behavior, as encoded in their reduced feature representations (energy signatures derived from mPOD projections; see Step 3 in Fig. 2). The method begins with a set of representative prototypes p_j, with $j \in \{1, 2, \dots, n_P\}$, each corresponding to a distinct free-surface behavior. This selection was first carried out manually and then refined iteratively. For every prototype, the leading spatial modes obtained from its mPOD decomposition are retained to encode its dominant flow features in a reduced form. The collection of these mode sets defines a global reference basis onto which all other cases are projected for subsequent clustering and classification.

Denoting by m_j the number of mPOD modes retained for prototype p_j, the global reference basis matrix is constructed as

$$\mathbf{\Phi}_{\text{ref}} = \left[\boldsymbol{\phi}_1^{(p_1)} \quad \dots \quad \boldsymbol{\phi}_{m_1}^{(p_1)} \quad \dots \quad \boldsymbol{\phi}_1^{(p_{n_P})} \quad \dots \quad \boldsymbol{\phi}_{m_{n_P}}^{(p_{n_P})} \right], \tag{14}$$

with $\mathbf{\Phi}_{\text{ref}} \in \mathbb{R}^{n_s \times n_b}$ and $n_b = \sum_{j=1}^{n_P} m_j$ the total number of basis vectors across all prototypes.

Given this reference basis, the snapshot matrix $\boldsymbol{D} \in \mathbb{R}^{n_s \times n_t}$ of any experimental realization - whether part of the training set or unseen—can be projected onto the reduced subspace through a standard linear projection:

$$\boldsymbol{A}_{\text{proj}} = (\mathbf{\Phi}_{\text{ref}}^{\top} \mathbf{\Phi}_{\text{ref}})^{-1} \mathbf{\Phi}_{\text{ref}}^{\top} \boldsymbol{D} \in \mathbb{R}^{n_b \times n_t}. \tag{15}$$

The resulting coefficient matrix $\boldsymbol{A}_{\text{proj}}$ provides a compact, physically interpretable representation of each realization in terms of its similarity to the prototype modes.

This operation linearly maps the videos $\boldsymbol{D} \in \mathbb{R}^{n_s \times n_t}$ into a set of n_b time series, stored in $\boldsymbol{A}_{\text{proj}} \in \mathbb{R}^{n_b \times n_t}$, with $n_b \ll n_t$, that quantify the temporal activation of each reference mode in Eq. (14). This is thus a compression $n_s \to n_b$ of each image in the video.

The following step consists of compressing the temporal dimension to $n_t \to 1$, which transforms each video into a compact feature vector $z_i \in \mathbb{R}^{n_b}$. This is carried out by first filtering the time series in $\boldsymbol{A}_{\text{proj}}$ using the same multi-resolution filter bank employed in the mPOD analysis, and then computing the ℓ_2-norm ($\|\cdot\|_2$) of each filtered time series.

Let $\boldsymbol{h}_m = [\, h_m[0],\ h_m[1], \dots,\ h_m[n_O - 1]\,]^{\top} \in \mathbb{R}^{n_O}$ denote the impulse response of the FIR filter associated with scale m, where $\tau = 0, 1, \dots, n_O - 1$ is the discrete time index and n_O is the filter order. The i-th time series $\boldsymbol{a}_i^{(p_j)} \in \mathbb{R}^{n_t}$, extracted from $\boldsymbol{A}_{\text{proj}}$, is then filtered using a zero-phase FIR operation. The filtered signal is evaluated at the discrete time index $k \in \{0, 1, \dots, n_t - 1\}$ and given by

$$a_{i,\text{filt}}^{(p_j)}[k] = \sum_{n=0}^{n_O-1} h_m[n] \left(\sum_{\tau=0}^{n_O-1} h_m[\tau]\, a_i^{(p_j)}[k + n - \tau] \right). \tag{16}$$

Here $\boldsymbol{a}_i^{(p_j)}$ is obtained through the projection on the prototype basis element $\boldsymbol{\phi}_i^{(p_j)}$, and $a_{i,\text{filt}}^{(p_j)}[k]$ is its filtered counterpart. The feature vector is then computed as

$$z_i = \left[\left\| \boldsymbol{a}_{1,\text{filt}}^{(p_1)} \right\|_2, \dots, \left\| \boldsymbol{a}_{m_1,\text{filt}}^{(p_1)} \right\|_2, \dots \left\| \boldsymbol{a}_{1,\text{filt}}^{(p_{n_P})} \right\|_2, \dots, \left\| \boldsymbol{a}_{m_{n_P},\text{filt}}^{(p_{n_P})} \right\|_2 \right]^{\top} \in \mathbb{R}^{n_b}. \tag{17}$$

The entries of this vector collect the similarity scores associated with all mPOD modes across all prototypes. To quantify the contribution of a specific prototype p_j to a given test case, the scores corresponding to its modes are grouped. Denoting by $\mathcal{I}_p$ the set of indices in z_i associated with prototype p_j, the prototype score is defined as

$$s_i^{(p_j)} = \|(z_i)_{\mathcal{I}_p}\|_2, \quad \tilde{s}_i^{(p_j)} = \frac{s_i^{(p_j)}}{\sum_{j=1}^{n_P} s_i^{(p_j)}}. \tag{18}$$

Feature vectors defined in Eq. (17), along with the prototype presence metrics in Eq. (18), are computed for all $i = 1, \ldots, N_{\mathrm{pts}}$ videos. Then, to identify the underlying sloshing regimes, an unsupervised clustering is performed in this reduced-order space using standard k-means clustering [73]. This algorithm partitions the set of feature vectors $\{z_i\}_{i=1}^{N_{\mathrm{pts}}}$ into K disjoint clusters $\{\mathcal{C}_0, \ldots, \mathcal{C}_{K-1}\}$ by minimizing the within-cluster variance, i.e., the distance between each point and its assigned cluster centroid:

$$\min_{\{\mathcal{C}_0,\ldots,\mathcal{C}_{K-1}\}} \sum_{c=0}^{K-1} \sum_{z_i \in \mathcal{C}_c} \|z_i - \boldsymbol{\mu}_c\|_2^2, \tag{19}$$

where $\boldsymbol{\mu}_c$ denotes the centroid of cluster $\mathcal{C}_c$. At each iteration, the centroid is updated by averaging the feature vectors belonging to the cluster:

$$\boldsymbol{\mu}_c = \frac{1}{|\mathcal{C}_c|} \sum_{z_i \in \mathcal{C}_c} z_i, \tag{20}$$

and the feature vector z_i is then reassigned to the cluster whose centroid is closest in the Euclidean sense:

$$z_i \in \mathcal{C}_c \quad \text{if} \quad \|z_i - \boldsymbol{\mu}_c\|_2^2 \leqslant \|z_i - \boldsymbol{\mu}_j\|_2^2, \quad \forall j = 0, \ldots, K-1. \tag{21}$$

To ensure that the final clustering is independent of the initial prototype selection, the entire procedure—from the prototype basis construction (14) to the clustering and score assignment (21)—is repeated iteratively. At each iteration, the new prototypes are defined as the medoids of the clusters, i.e., the realizations minimizing the intracluster Euclidean distance in the reduced feature space. The iterative process continues until convergence, defined as either (i) an adjusted Rand index (ARI) between consecutive clusterings exceeding a prescribed threshold (here ARI $\geqslant$ 0.98) [74], or (ii) no change in the medoid set relative to the previous iteration (prototype overlap). The final cluster labels obtained upon convergence are then used in the classification stage.

D. Regime classification via physics-informed SVM

The proposed regime-classification strategy employs a physics-informed SVM to delineate the boundaries between the sloshing regimes identified through clustering, as shown in Step 4 of Fig. 2. The SVM [75] provides a supervised mapping from the labeled experimental realizations onto the nondimensional parameter space:

$$\boldsymbol{x}_i = \begin{bmatrix} A_f/R \\ \omega_f/(2\,\omega_{1,0}) \end{bmatrix} \in \mathbb{R}^2, \tag{22}$$

enabling prediction of the expected regime for new operating conditions. Physical consistency is introduced through a weighting scheme that incorporates analytical stability information from the Mathieu-equation Floquet analysis, yielding a hybrid framework that blends data-driven classification with the governing physics of parametric resonance (see Sec. VI E).

The experimental campaign yields a dataset of N_{pts} samples: $\boldsymbol{x}_1, \ldots, \boldsymbol{x}_{N_{\mathrm{pts}}}$. For each sample, the prototype-based clustering method of Sec. V C assigns a label $\mathcal{C}_0, \ldots, \mathcal{C}_{K-1}$ corresponding to a distinct sloshing regime. The objective of the classification step is to construct a continuous decision function $f(\boldsymbol{x}) : \boldsymbol{x} \to \{\mathcal{C}_0, \ldots, \mathcal{C}_{K-1}\}$ that generalizes to unseen data and provides smooth decision boundaries between regimes. Following the one-vs-one (OvO) strategy [76,77] adopted here, $K(K-1)/2$ binary SVM classifiers are trained, each separating a unique pair of classes. During inference, their pairwise decision functions are aggregated into per-class scores $\boldsymbol{F}_i = [\, f_{i0},\ f_{i1}, \ldots, f_{i,K-1}\,]$, where each f_{ik} encodes the combined vote and margin confidence for class k.

Each binary classifier is defined by a kernel-based decision function

$$f(\boldsymbol{x}) = \sum_{i=1}^{N_s} \alpha_i y_i\, \mathcal{K}(\boldsymbol{x}_i, \boldsymbol{x}) + b, \tag{23}$$

where N_s denotes the number of support vectors [i.e., the training samples with $\alpha_i > 0$ after solving the dual problem in Eqs. (27) and (28)], α_i and b are learned coefficients, $y_i \in \{-1, +1\}$ are binary class labels, $\boldsymbol{x}_i$ are the corresponding support vectors, and $\mathcal{K}(\boldsymbol{x}, \boldsymbol{x}')$ is a kernel function measuring similarity in the input space. A third-order polynomial kernel is used:

$$\mathcal{K}(\boldsymbol{x}, \boldsymbol{x}') = (\gamma\, \boldsymbol{x}^\top \boldsymbol{x}' + c)^3, \tag{24}$$

with γ controlling the influence of individual training points and c the bias term. The hyperparameters are set to $\gamma = 1/(2\ \mathrm{var}(\boldsymbol{x}))$, $c = 5$, and penalty parameter $C = 3$.

The classification uncertainty is then quantified through a top-margin-based criterion that compares the two highest decision scores in $\boldsymbol{F}_i$. Sorting the scores as $f_{i(1)} \geqslant f_{i(2)} \geqslant \cdots \geqslant f_{i(K)}$ the confidence gap is defined as

$$g_i = f_{i(1)} - f_{i(2)}, \quad g_i \geqslant 0, \tag{25}$$

which quantifies the separation between the most probable class and its nearest competitor. Across the parametric space, the gap is normalized to [0, 1] and inverted to yield the uncertainty measure

$$u_i = 1 - \frac{g_i - g_{\min}}{g_{\max} - g_{\min}}, \tag{26}$$

with $g_{\min}$ and $g_{\max}$ denoting the minimum and maximum gap values. Thus, large u_i values mark regions of low classifier confidence, typically near decision boundaries. A quantile threshold of 2.5% is applied, retaining only the uppermost uncertain points to delineate these regions.

The Support Vector Machine used here follows the weighted formulation implemented in `scikit-learn`. For a given OvO classifier, let N denote the number of training samples belonging to the two classes being separated. The dual optimization problem solves for the multipliers $\boldsymbol{\alpha} = [\alpha_1, \ldots, \alpha_N]^\top$ and the bias b via

$$\min_{\boldsymbol{\alpha}} \quad \tfrac{1}{2}\, \boldsymbol{\alpha}^\top \mathbf{Q}\, \boldsymbol{\alpha} - \mathbf{1}^\top \boldsymbol{\alpha}, \tag{27}$$

$$\text{s.t.} \quad 0 \leqslant \alpha_i \leqslant C\, w_i, \quad \sum_{i=1}^{N} y_i\, \alpha_i = 0, \tag{28}$$

where $Q_{ij} = y_i y_j\, \mathcal{K}(\boldsymbol{x}_i, \boldsymbol{x}_j)$ for $i, j = 1, \ldots, N$, $C > 0$ is the penalty parameter, and w_i are sample-specific weights. After optimization, the subset of training samples with $\alpha_i > 0$ constitute the support vectors in Eq. (23). The bias b is recovered from the Karush-Kuhn-Tucker conditions.

To encode prior physical knowledge, the weights w_i are derived from the analytical neutral-stability boundaries of the inviscid Mathieu equation (Sec. III). Near these boundaries, the dynamics transition between stable and unstable behavior, increasing classification uncertainty.

For each sample, the Euclidean distance d_i to the theoretical boundary is computed by orthogonal projection onto the boundary curve, and a normalized measure

$$t_i = \mathrm{clip}\left(\frac{d_i - \delta_1}{\delta_2 - \delta_1},\ 0,\ 1\right) \tag{29}$$

is used to define individual weights:

$$w_i = w_{\min} + (1 - w_{\min})\, t_i. \tag{30}$$

Here, δ_1 and δ_2 specify the inner and outer limits of a guard band, and $w_{\min}$ sets the minimum confidence assigned to near-boundary samples. The operator $\text{clip}(x, a, b) = \min(\max(x, a), b)$ denotes elementwise bounding to the interval $[a, b]$.

Weights are then normalized and clipped to avoid extreme scaling:

$$w_i \leftarrow \text{clip}\left(\frac{w_i}{\overline{w}},\ c_{\min},\ c_{\max}\right), \tag{31}$$

where $\overline{w}$ is the mean weight over the training set. With $\delta_1 = 0.01$, $\delta_2 = 0.10$, $w_{\min} = 0.01$, and $(c_{\min}, c_{\max}) = (0.1, 5.0)$, this penalization scheme downweights samples close to the theoretical boundaries, guiding - but not constraining - the classifier toward physically consistent decision regions.

VI. RESULTS

The results are organized into four subsections, each analyzing a distinct stage of the proposed methodology (see Fig. 2), leading to the final sloshing regime map. For clarity, Secs. VI A–VI D illustrate the complete workflow using the intermediate fill level $H_l/D = 0.50 \pm 0.04$, while Sec. VI E presents the final regime maps for all tested fill ratios $H_l/D \in [0.40; 0.67]$.

For the case $H_l/D = 0.50$, a total of 73 test points were investigated through 146 runs to ensure repeatability (see Table I). The forcing amplitude spanned $A_f/R \in [0.02, 0.62]$ and $A_f\omega_f^2/g \in [0.02, 0.77]$, while the forcing frequency ratio covered $\omega_f/(2\,\omega_{1,0}) \in [0.90, 1.20]$. The natural frequency of the first longitudinal sloshing mode was identified as $\omega_{1,0} \approx 6.08\,\text{rad s}^{-1}$ from free-decay tests, as detailed in Sec. VI A.

A. Natural frequency and damping ratio

The natural frequency $\omega_{1,0}$ and damping ratio $\zeta_{1,0}$ of the antisymmetric longitudinal mode ($m = 1,\ n = 0$) were obtained from the free-decay tests following the methodology in Sec. V A. Once the external excitation was removed, the tank–fluid system exhibited undriven oscillations dominated by a single mode, confirming that the extracted parameters correspond to a dominant (1,0) response rather than a multimodal superposition.

Figure 3 shows the three leading mPOD modes for $H_l/D = 0.50$ at $A_f = 39.7\,\text{mm}$ and $f_f = 1.85\,\text{Hz}$, including their spatial structures $\boldsymbol{\phi}_r$, temporal coefficients $\boldsymbol{\psi}_r$ with Hilbert envelopes $\mathcal{H}_i$, and frequency spectra $|\hat{\boldsymbol{\psi}}_r|$. The leading spatial mode $\boldsymbol{\phi}_1$ is antisymmetric, with a nodal line at $x/L = 0$ and antinodes at $x/L = \pm 0.5$, matching the expected sloshing eigenmode $(m, n) = (1, 0)$ shape [49].

After the onset of motion at $t = 0.0\,\text{s}$, the temporal coefficient $\boldsymbol{\psi}_1$ grows exponentially and reaches a limit-cycle oscillation at $t \approx 7.5\,\text{s}$. The spectrum shows a dominant frequency at $f \approx 0.93\,\text{Hz}$, corresponding to the 1/2-subharmonic of the driving frequency and confirming a Faraday-type instability with liquid oscillation at half the forcing frequency. Between $t = 60.0\,\text{s}$ and $t = 65.0\,\text{s}$, the imposed motion was exponentially attenuated to prevent excitation of higher-order modes, with the fully free decay starting at $t \sim 65.0\,\text{s}$.

Figure 4 displays the time-frequency representation of the three temporal coefficients ($\boldsymbol{\psi}_1$, $\boldsymbol{\psi}_2$, and $\boldsymbol{\psi}_3$) in Fig. 3, the two load-cell vertical signals (F_{z_1}, F_{z_2}), and the vertical acceleration (a_z) over the interval $t \in [-5.0, 90.0]$ seconds. The vertical frequency axis is normalized by the forcing frequency f_f, emphasizing the drive and its (sub)harmonics. Power is shown in decibels as $P_{\log}(t, f) = 10\log_{10}(|W(t, f)|^2/|W(t, f)|^2_{\max})$, where $W(t, f)$ denotes the CWT coefficient.

In the force spectra ($f_{F_{z_1}}/f_f$ and $f_{F_{z_2}}/f_f$), a dominant ridge appears at the driving frequency while the excitation is active, due to the combined inertia of the liquid and tank. Once parametric sloshing develops, a weaker ridge emerges at $t \approx 7.5\,\text{s}$ near $f_f/2$, indicating the onset of the expected Faraday-type subharmonic response associated with the (1,0) mode. A $3f_f/2$ sideband also appears, arising from nonlinear coupling between the drive and the subharmonic oscillation.

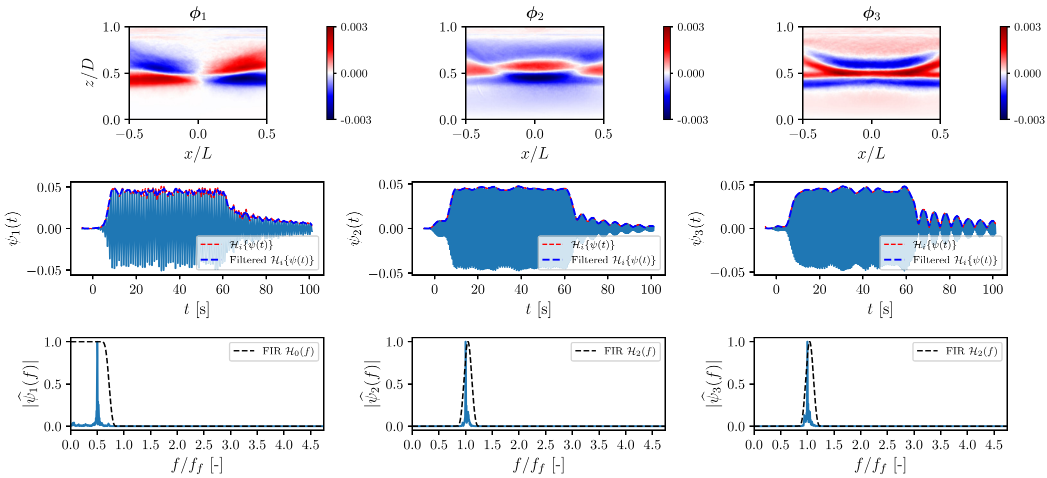

FIG. 3. mPOD analysis for $H_l/D = 0.50$ at $A_f = 39.7$ mm and $f_f = 1.85$ Hz performed over $t \in [-5.0,\ 100.0]$ s. The spatial modes $\boldsymbol{\phi}_r$ capture the dominant coherent free-surface deformations, and $\boldsymbol{\psi}_r$ are their temporal coefficients. The frequency spectra $|\widehat{\boldsymbol{\psi}}_r|$ are normalized by their peak amplitude. The three leading modes ($\boldsymbol{\phi}_1$, $\boldsymbol{\phi}_2$, $\boldsymbol{\phi}_3$) use individual zero-centered symmetric diverging color scales, with limits set by each mode's maximum absolute amplitude. Excitation starts at $t = 0.0$s. The dominant mode $\boldsymbol{\phi}_1$ shows an antisymmetric longitudinal structure with a mid-length nodal line and end antinodes, characteristic of $(m, n) = (1, 0)$, with a subharmonic response at $f_f/2$.

The accelerometer spectra (f_{a_z}/f_f) display only the primary forcing frequency, as expected for the rigid-body motion, while the subharmonic ridge persists in F_{z_1}, F_{z_2}, and $\boldsymbol{\psi}_1$, confirming the link between image-derived and measured quantities. Nonlinear coupling in $\boldsymbol{\psi}_1$ is also evidenced by mild spectral broadening and weak sidebands. At $t \sim 65.0$ s, a slight upward shift of the subharmonic ridge marks the transition to the free-decay phase. This ridge remains active at nearly constant frequency, while its power decays as viscous effects damp the motion. Since the damping is weak ($\zeta_{m,n} \ll 1$), the undamped and damped natural frequencies are nearly identical, $\omega_{m,n} \approx \omega_{d_{m,n}}$ [6]. For this test case, the subharmonic ridge is consistent across $\boldsymbol{\psi}_1$, F_{z_1}, and F_{z_2}, giving a mean damped frequency $\bar{f}_{d_{1,0}} \approx 0.525 f_f$ or $\bar{f}_{d_{1,0}} \approx 0.97$ Hz.

To achieve robust results the damped natural frequency extraction is repeated across three additional independent tests (following the methodology above), where $\boldsymbol{\phi}_1$ highlights the targeted mode ($m = 1,\ n = 0$); within each test, the three measurement methods (mPOD mode and the two load cells) are considered correlated and are therefore first averaged to provide a single per-test estimate. At $H_l/D = 0.50$, these additional test cases were performed at $A_f = \{28.4,\ 32.2,\ 36.7\}$ mm and $f_f = \{1.84,\ 2.04,\ 1.94\}$ Hz, respectively, and are also used in the sloshing maps proposed in Sec. VI E. Statistical uncertainty on the mean was quantified with a two-sided 95% Student's t-interval based on the standard error $s/\sqrt{N}$, where s is the unbiased standard deviation. This yields a conservative pooled estimate of $\bar{f}_{d_{1,0}} = 0.97 \pm 0.03$ Hz (95% CI; $N = 4$), such that $\bar{\omega}_{d_{1,0}} \approx 6.08$ rad s^{-1}. Analysis of the load-cell spectra during the free-decay period ($t > 67.5$ s) reveals a clear single ridge, while the temporal coefficient $\boldsymbol{\psi}_1$ shows slight amplitude modulation instead of a smooth exponential decay [see Figs. 3 and 4(a)]. This modulation produces a weak beating pattern, making the raw $\boldsymbol{\psi}_1$ signal unsuitable for direct damping estimation using classical approaches such as the logarithmic decrement [4,78] or Hilbert-envelope methods [19,20] without prior band-pass filtering.

Figure 5 summarizes the damping identification procedure applied to $\boldsymbol{\psi}_1$, F_{z_1}, and F_{z_2}. The top row shows the dominant wavelet ridge frequency, with a vertical marker indicating the instant when the subharmonic ridge power surpasses the forced response, marking the onset of free decay. For this

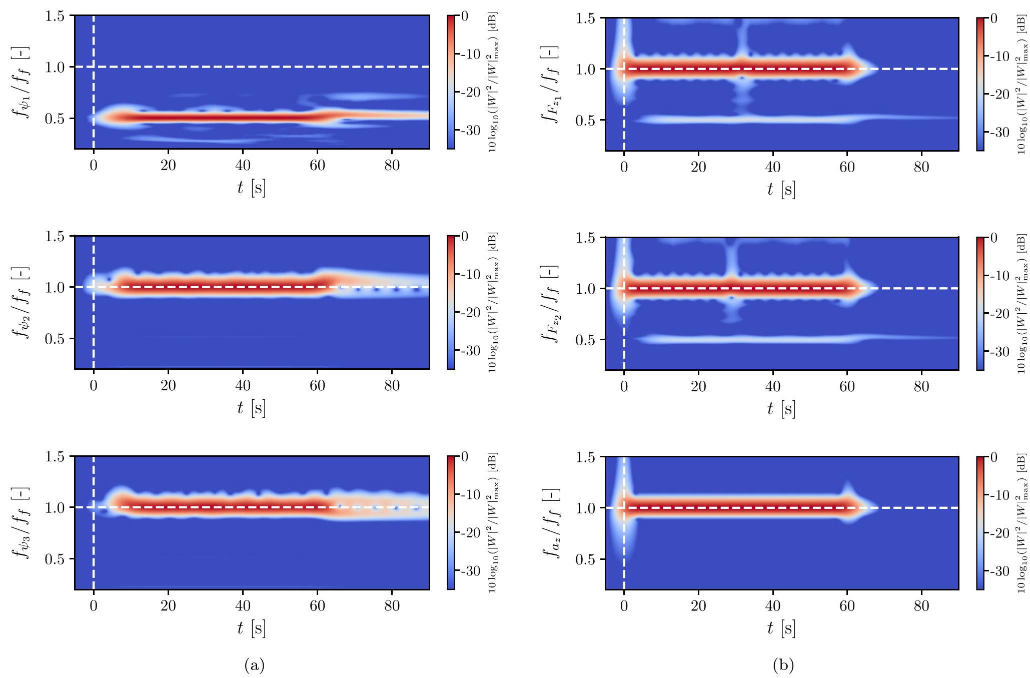

FIG. 4. Wavelet scalograms (time–frequency representation) obtained from the complex Morlet transform (bandwidth 6.0, center frequency 2.0) of the temporal coefficients of the three most energetic POD modes ($\boldsymbol{\psi}_1$, $\boldsymbol{\psi}_2$ and $\boldsymbol{\psi}_3$) in Fig. 3, the two load-cell force signals (F_{z_1} and F_{z_2}), and the accelerometer (a_z) over the interval $t \in [-5.0, 90.0]$ seconds. The sloshing signal is initiated at $t = 0.0$s. The frequency axis is normalized by the forcing frequency $f_f = 1.85$ Hz. In each panel, the Wavelet-coefficient power is represented on a relative logarithmic scale as $10\log_{10}(|W|^2/|W|^2_{\mathrm{max}})$, so that 0 dB corresponds to the maximum response. (a) mPOD temporal coefficients: ψ_1, ψ_2, and ψ_3. (b) Sensor signals: F_{z1}, F_{z2}, and a_z.

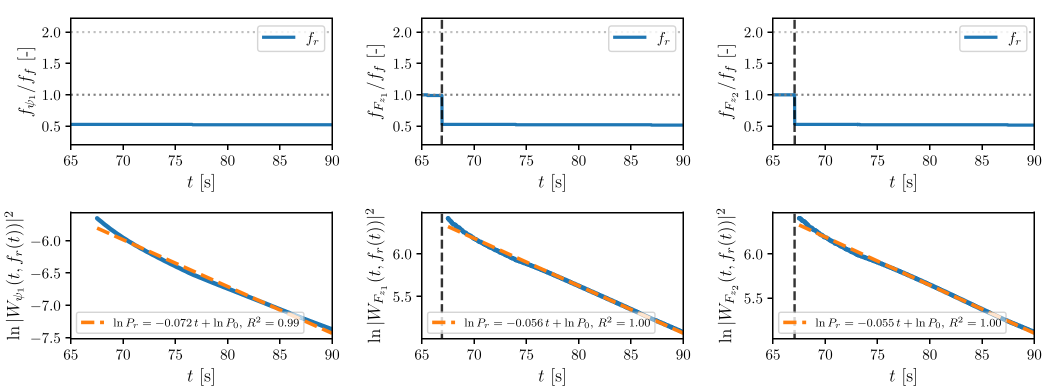

FIG. 5. Wavelet ridge diagnostics for $H_l/D = 0.50$ at $A_f = 39.7$ mm and $f_f = 1.85$ Hz. Columns correspond to the three signals ($\boldsymbol{\psi}_1$, F_{z_1}, F_{z_2}). Top row: ridge frequency $f_r(t)/f_f$ identified as $\arg\max_{f\in\mathcal{B}} P(t, f)$; the dashed vertical lines indicate ridge jumps. Bottom row: logarithmic ridge power $\ln P_r(t)$ with least-squares fit $\ln P_r(t) = m_{\ln P_r}\, t + P_0$ over the ring-down window [67.5, 90.0] (reported $m_{\ln P_r} = -2\zeta_{1,0}\omega_{1,0}$ and R^2 shown in each panel).

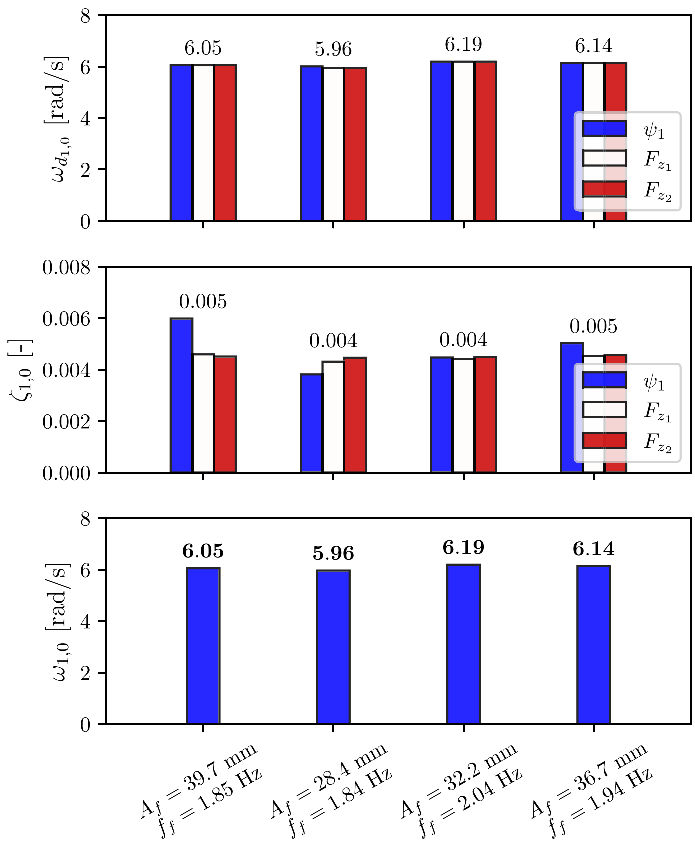

FIG. 6. Damped natural frequency $\omega_{d_{1,0}}$, damping ratio $\zeta_{1,0}$, and undamped natural frequency $\omega_{1,0}$ of the antisymmetric sloshing mode ($m = 1,\ n = 0$), estimated from the leading mPOD coefficient $\boldsymbol{\psi}_1$ and the vertical forces F_{z_1} and F_{z_2}. Results correspond to four free-decay tests with $A_f = \{39.7,\ 28.4,\ 32.2,\ 36.7\}$ mm and $f_f = \{1.85,\ 1.84,\ 2.04,\ 1.94\}$ Hz. Mean values for each test are shown as bar groups.

case ($A_f = 39.7$ mm, $f_f = 1.85$ Hz), the transition occurs at $t \approx 66$ s, consistent with Fig. 4, and the fitting window was set to $t_1 = 67.5$ s and $t_2 = 90.0$ s. The bottom row presents the logarithmic ridge power $\ln P_r(t)$ and the corresponding linear least-squares fit. The high coefficients of determination ($R^2 \geqslant 0.99$) confirm that a single exponentially decaying mode was successfully isolated, with $\boldsymbol{\phi}_1$ validating the expected $(m, n) = (1, 0)$ structure.

Figure 6 compiles the estimates of the damped and undamped natural frequencies and the damping ratios obtained across the four independent tests ($N = 4$). The mean damping ratio is $\bar{\zeta}_{1,0} = 0.004 \pm 0.001$, determined using the same CWT-based ridge analysis employed for the damped frequency. The undamped natural frequency for each test was then computed as $\omega_{1,0_i} = \omega_{d_{1,0_i}} / \sqrt{1 - \zeta_{1,0_i}^2}$, with $i = 1, \ldots, 4$, and the average taken with a two-sided 95% Student's t-interval, yielding $\bar{\omega}_{1,0} = 6.08 \pm 0.16\,\mathrm{rad\,s^{-1}}$ (see Table II). Consistent with previous studies [4,78,79], this low-order sloshing mode exhibits a small damping ratio, validating the approximation $\bar{\omega}_{1,0} \approx \bar{\omega}_{d_{1,0}}$ for the present horizontal geometry.

B. Prototype library

The image sequences over $t \in [0, 60]$ s were analyzed at a down-sampled rate of 17.5 Hz ($n_t = 1050$), after spatial cropping to center the tank ($n_x = 1900$, $n_z = 1185$). Six representative

TABLE II. Statistical summary of the free-decay estimates of the fundamental antisymmetric sloshing mode ($m = 1,\ n = 0$) at $H_l/D = 0.50$. Reported are the forcing amplitude A_f, forcing frequency f_f, per test mean damped frequency $\bar{f}_{d_{1,0}}$, damped angular frequency $\bar{\omega}_{d_{1,0}}$, damping ratio $\bar{\zeta}_{1,0}$, and the averaged natural frequency $\bar{\omega}_{1,0}$ with a 95% confidence interval based on $N = 4$ tests.

A_f [mm]	f_f [Hz]	$\bar{f}_{d_{1,0}}$ [Hz]	$\bar{\omega}_{d_{1,0}}$ [rad s^{-1}]	$\bar{\zeta}_{1,0}$ [−]	$\bar{\omega}_{1,0}$ [rad s^{-1}] (95% CI; $N = 4$)
39.7	1.85	0.96	6.05	0.005	
28.4	1.84	0.95	5.96	0.004	6.08 ± 0.16
32.2	2.04	0.99	6.19	0.004	
36.7	1.94	0.98	6.14	0.005	

prototypes ($n_P = 6$), each described by its three leading mPOD modes ($m_j = 3$), were selected to compactly represent the main recurrent free-surface response families near $2\,\omega_{1,0}$: stable, dominant longitudinal, higher-order, and mixed-mode states. These prototypes define the reference basis $\boldsymbol{\Phi}_{\mathrm{ref}}$, used to compare all test realizations by their modal resemblance to the dominant sloshing responses and to compute the energy-based quantities for subsequent clustering.

Figures 7 and 8 present the selected prototypes, each displayed with its spatial mode shapes $\boldsymbol{\phi}_{m_k}^{(p_j)}$, temporal coefficients $\boldsymbol{\psi}_{m_k}^{(p_j)}(t)$ and their Hilbert-transform envelopes, as well as the corresponding frequency spectra $|\hat{\boldsymbol{\psi}}_{m_k}^{(p_j)}|$ and the transfer functions $\mathcal{H}_m$ of the filters that identify each mode. The forcing amplitude and frequency for every test are indicated in the subplot labels.

All prototypes in Fig. 7 correspond to the resonance condition $\omega_f = 2\,\omega_{1,0}$. Across the three cases, the dominant temporal coefficient exhibits a subharmonic peak at $\omega/(2\omega_{1,0}) \approx 0.5$, corresponding to $\omega \approx \omega_{1,0} \approx \omega_f/2$ near the principal parametric resonance. Prototype p_1, shown in Fig. 7(a) at $A_f/R = 0.02$, represents a stable free-surface response. The spatial structure $\boldsymbol{\phi}_1^{(p_1)}$ shows limited projection onto the longitudinal mode, with oscillations localized near the back and front contact lines, which remain visible due to the camera position slightly above the free surface (see Fig. 2). The corresponding temporal coefficient decays monotonically, consistent with the Hilbert-transform envelope, indicating that the system remains below the instability threshold.

Prototype p_2, with $A_f/R = 0.13$, exhibits a longitudinal response that grows from an initial transient and saturates into a periodic state. The spatial structure $\boldsymbol{\phi}_1^{(p_2)}$ shows a single nodal line at the tank mid-plane, located at approximately $x/L \approx 0.0$, identified by the zero crossing in the color map separating regions of opposite phase, together with two antinodes near the tank ends ($x/L = \pm 0.5$). This pattern corresponds to the first antisymmetric longitudinal mode [49]. The corresponding temporal coefficient, $\boldsymbol{\psi}_1^{(p_2)}$, reaches a limit cycle, indicating a subharmonic sloshing response associated with the onset of the ($m = 1,\ n = 0$) parametric resonance.

Prototype p_3, at $A_f/R = 0.33$, exhibits a longitudinal pattern similar to that of p_2, with increased modal amplitude as indicated by the contrast in the color map. The oscillation converges to a limit cycle, reaching saturation at approximately $t \approx 10$ s, as shown by the leading temporal coefficient $\boldsymbol{\psi}_1^{(p_3)}$. The corresponding spatial structure $\boldsymbol{\phi}_1^{(p_3)}$ retains a single nodal line at mid-span, confirming the persistence of the ($m = 1,\ n = 0$) mode. The interface profile exhibits increased curvature, consistent with nonlinear effects at higher forcing amplitude.

Figure 8 introduces prototypes p_4 through p_6, which correspond to sloshing responses involving higher-order and mixed-mode dynamics. Prototype p_4, measured at $A_f/R = 0.40$ and $\omega_f/(2\,\omega_{1,0}) = 1.17$, is shown in Fig. 8(a). The leading spatial structure, $\boldsymbol{\phi}_1^{(p_4)}$, exhibits a symmetric higher-order longitudinal pattern with nodal locations near $x/L \approx -0.5$, $x/L \approx 0.0$, and $x/L \approx 0.5$, together with antinodes around $x/L \approx \pm 0.25$. This structure is consistent with a dominant ($m = 3, n = 0$)-type

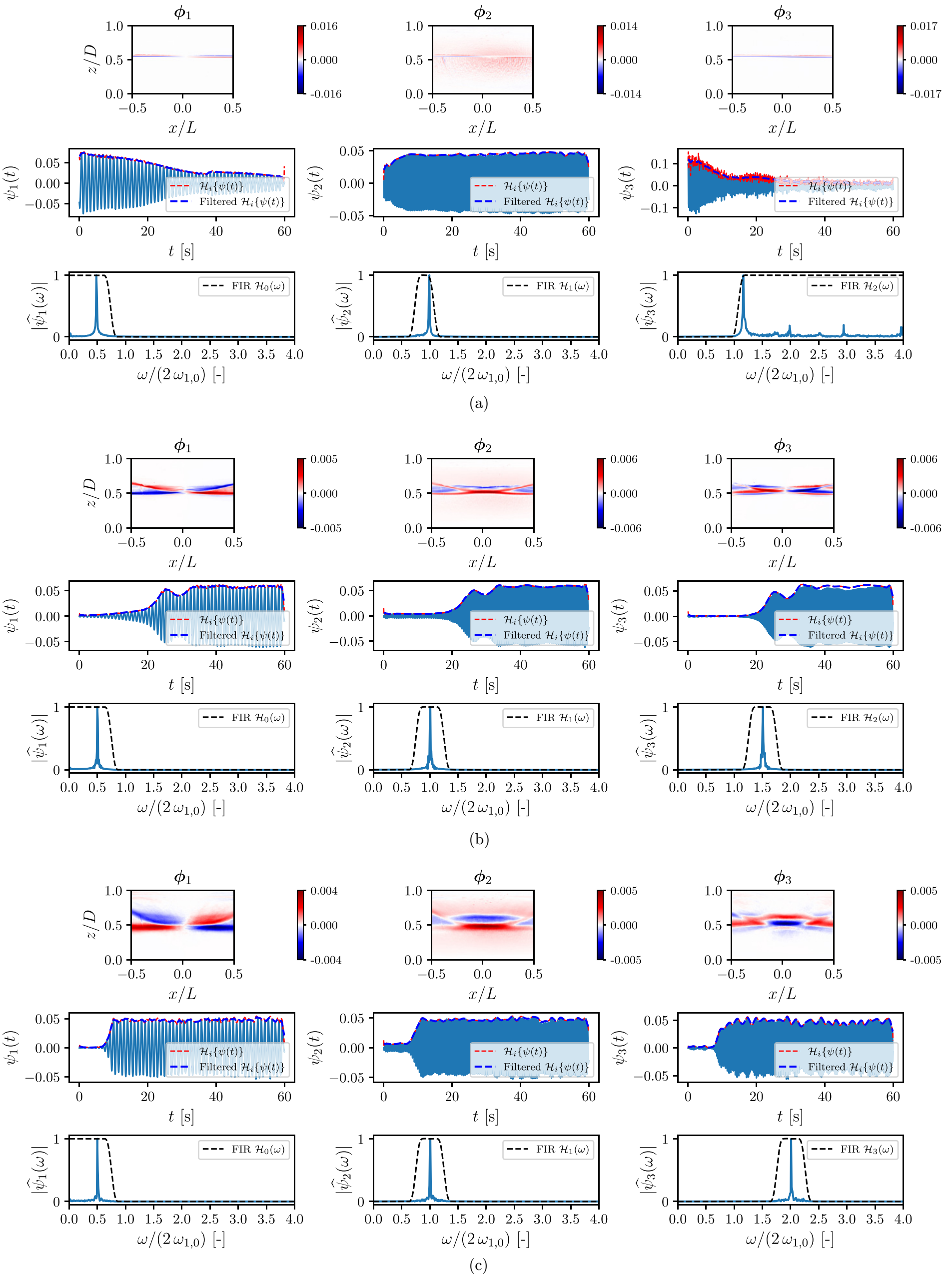

FIG. 7. mPOD spatial structures $\boldsymbol{\phi}_{m_k}$, normalized frequency spectra $|\hat{\boldsymbol{\psi}}_{m_k}|$ with overlaid FIR filters $\mathcal{H}_m$, and temporal structures $\boldsymbol{\psi}_{m_k}$ for three prototype references p_1 to p_3, each characterized by longitudinal sloshing dynamics ($m = 1, n = 0$). The spatial modes are shown using individual zero-centered symmetric diverging color bars, with limits set by the maximum absolute modal amplitude of each mode. (a) Prototype p_1: $A_f/R = 0.02$, $\omega_f/(2\omega_{1,0}) = 1.00$. (b) Prototype p_2: $A_f/R = 0.13$, $\omega_f/(2\omega_{1,0}) = 1.00$. (c) Prototype p_3: $A_f/R = 0.33$, $\omega_f/(2\omega_{1,0}) = 1.00$.

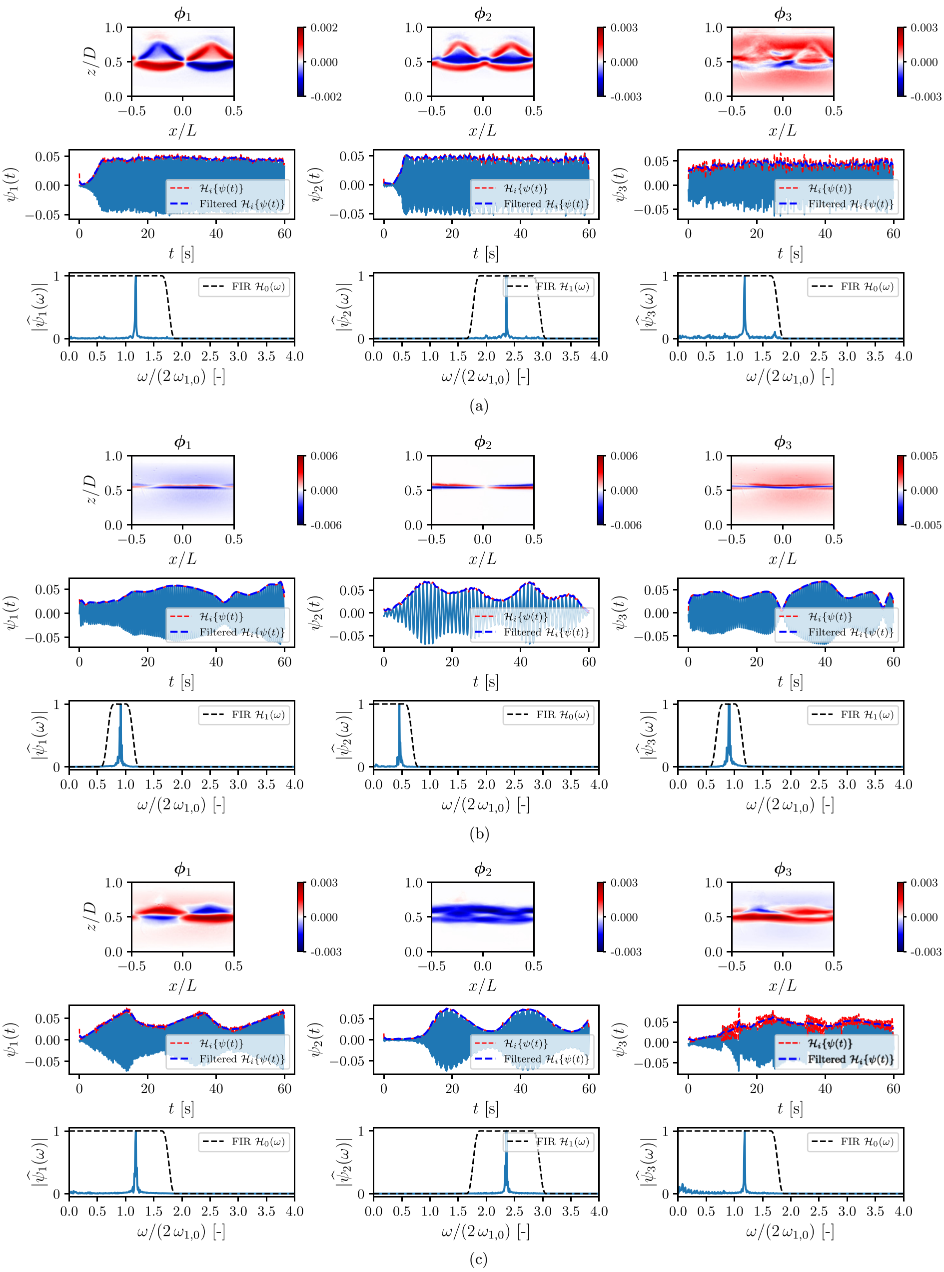

FIG. 8. Same as Fig. 7 but considering the prototypes p_4 to p_6, characterized by high-order longitudinal dynamics $(m = 2, n = 0)$ and $(m = 3, n = 0)$, with mixed-mode conditions in p_5 and p_6. (a) Prototype p_4: $A_f/R = 0.40$, $\omega_f/(2\omega_{1,0}) = 1.17$. (b) Prototype p_5: $A_f/R = 0.41$, $\omega_f/(2\omega_{1,0}) = 0.91$. (c) Prototype p_6: $A_f/R = 0.25$, $\omega_f/(2\omega_{1,0}) = 1.17$.

response. The corresponding temporal coefficient, $\boldsymbol{\psi}_1^{(p_4)}$, undergoes transient growth for $t < 10$ s and then reaches a sustained amplitude, indicating the establishment of a higher-order standing wave.

Prototype p_5, obtained at $A_f/R = 0.41$ and $\omega_f/(2\,\omega_{1,0}) = 0.91$, is shown in Fig. 8(b). Its spatial modes remain predominantly longitudinal, but $\boldsymbol{\phi}_1^{(p_5)}$ departs from the single-node

$(m = 1, n = 0)$ structure. Two nodal locations are observed at approximately $x/L \approx \pm 0.3$, indicating the contribution of a higher-order longitudinal component compatible with an $(m = 2, n = 0)$-type structure. The temporal coefficients exhibit amplitude modulation, indicating the onset of mixed-mode behavior, where the response is not dominated by a single longitudinal mode.

Finally, prototype p_6, obtained at $A_f/R = 0.25$ and $\omega_f/(2\,\omega_{1,0}) = 1.17$, shown in Fig. 8(c), exhibits a mixed-mode response with an additional transverse contribution. While the dominant spatial structure retains a higher-order longitudinal organization, it closely resembles $\boldsymbol{\phi}_1^{(p_4)}$ and is therefore consistent with a longitudinal $(m = 3, n = 0)$-type response. The secondary mode $\phi_2^{(p_6)}$ suggests transverse free-surface motion, indicating that the dynamics are no longer governed by a purely longitudinal standing-wave pattern. The corresponding temporal coefficients exhibit persistent amplitude modulation, but their spectra retain well-defined narrow-band peaks, consistent with a coherent mixed longitudinal-transverse oscillatory regime.

Overall, the six prototypes span the main observed free-surface responses, from a stable below-threshold state (p_1), to subharmonic longitudinal oscillations (p_2–p_3), and to higher-order or mixed-mode responses away from the primary resonance region (p_4–p_6). This reference basis is then used to project each test realization [using Eq. (15)] and compute the activation energies employed for regime clustering [see Eq. (17)]. The modal structures extracted by the mPOD remain well separated into longitudinal and transverse components and retain the dominant features required to classify the observed sloshing into physically meaningful regimes.

C. Similarity maps

Figure 9 displays similarity maps across the dimensionless forcing space for the six prototypes introduced in the previous subsection. These prototypes define reference families of free-surface responses spanning the reduced basis Φ_{ref}. Each test realization is projected onto this basis to quantify the contribution of each prototype, so that the maps indicate which response dominates under each forcing condition. These reduced-order signatures are then used in the clustering step to group cases with similar modal content.

The similarity score at each point is computed in step 3 of the proposed workflow (see Fig. 2) from the normalized energy signature. The projection in Eq. (15) is performed on a low-order reconstruction of each video, retaining the first $n_R = 30$ mPOD modes. In this way, the mPOD basis acts both as a decomposition and as a frequency-selective filter. The resulting maps reveal distinct regions associated with the activation of each prototype, organizing the free-surface responses across the forcing space.

In the lower part of the map $\tilde{s}_i^{(p_1)}$, prototype p_1 dominates, indicating that low forcing amplitudes correspond to nearly quiescent or weakly perturbed free-surface states. As the forcing amplitude increases ($A_f/R > 0.1$), the dominant similarity shifts toward prototype p_2 (see $\tilde{s}_i^{(p_2)}$), marking the onset of the fundamental longitudinal response slightly below the primary parametric resonance. A further increase in forcing leads to a transition toward prototype p_3 (see $\tilde{s}_i^{(p_3)}$), representative of large-amplitude longitudinal dynamics.

Prototype p_5, associated with mixed low-amplitude longitudinal dynamics [see Fig. 8(b)], exhibits partial overlap with prototypes p_1 and p_2, as indicated by the map $\tilde{s}_i^{(p_5)}$. This overlap reflects a continuous transition from stable conditions to weak longitudinal oscillations, with a narrow transitional region near $A_f/R \approx 0.1$. This behavior highlights the ability of the prototype-based representation to capture gradual changes in modal content across the forcing space.

In contrast, prototypes p_3, p_4, and p_6 remain clearly separated, each defining a distinct region of influence. The similarity distributions $\tilde{s}_i^{(p_4)}$ and $\tilde{s}_i^{(p_6)}$, both associated with higher-order longitudinal dynamics ($m = 3$), indicate a secondary instability region characterized by mode interaction and mixed-mode responses (see [32,40,61]). Interestingly, this region develops along a slope identical to that of $\tilde{s}_i^{(p_2)}$ and $\tilde{s}_i^{(p_5)}$, suggesting the presence of an instability tongue.

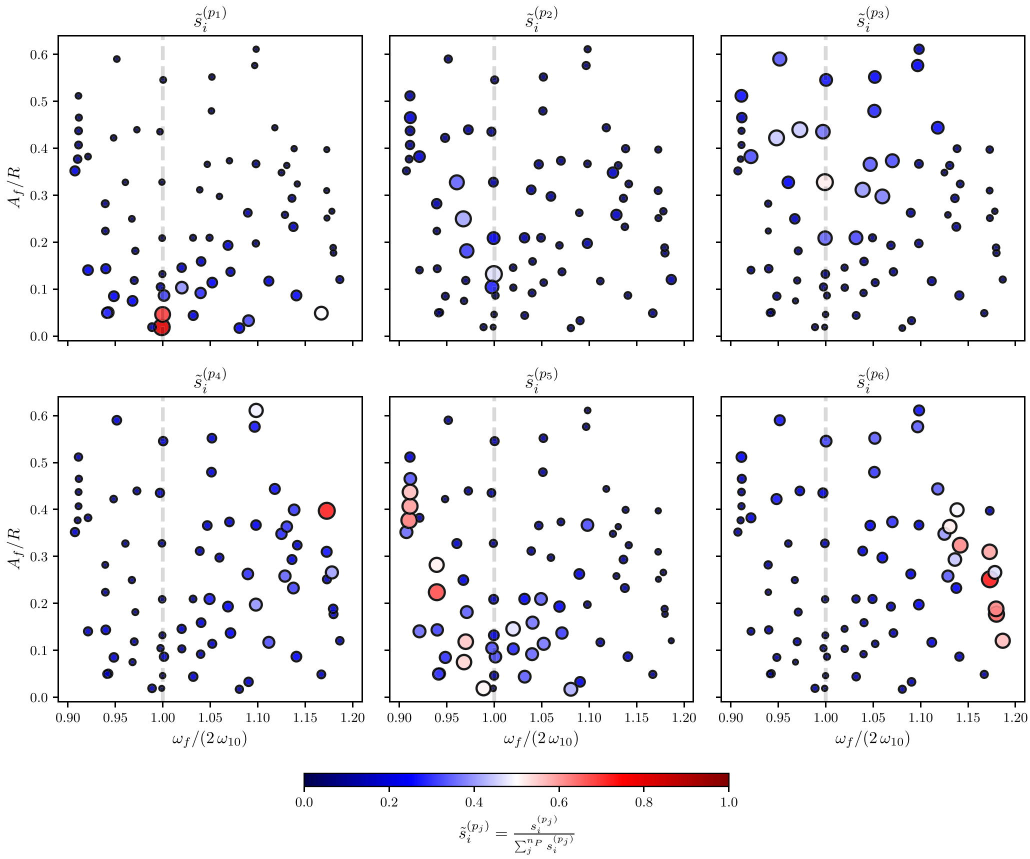

FIG. 9. Similarity maps of the prototypes shown in Figs. 7 and 8 for $H_l/D = 0.5$ in the dimensionless forcing space defined by the frequency ratio $\omega_f/(2\,\omega_{1,0})$ and amplitude ratio A_f/R. Each marker represents a test condition; its color indicates the normalized similarity score $\tilde{s}_i^{(p_j)} = s_i^{(p_j)} / \sum_{j=1}^{n_P} s_i^{(p_j)}$ defined in Eq. (18), and its size is proportional to that score.

D. Clustering and regime classification

This subsection discusses the clusters identified as recurrent classes of free-surface dynamics within the dimensionless forcing plane (A_f/R; $\omega_f/(2\,\omega_{1,0})$). The final labels, $\{\mathcal{C}_0, \ldots, \mathcal{C}_5\}$, shown in Fig. 10, are obtained using the unsupervised k-means algorithm applied to feature vectors extracted over the analyzed time interval ($t \in [0, 60]$ s). These clusters emerge from grouping test cases with similar free-surface signatures. The bar plots for the cluster medoids provide supporting evidence for the physical interpretation of each regime.

Figure 11 displays representative raw images (Step 1; see Fig. 2) at $t \approx 40$ s for each cluster medoid, providing a direct visualization of the associated free-surface dynamics. Several regimes exhibit highly complex interface behavior, including wave breaking, droplet ejection, and splashing, resulting in fragmented and irregular free-surface structures. In such conditions, a consistent reconstruction and tracking of the gas-liquid interface is extremely challenging. These images are shown for illustration only, as the cluster labels are determined from feature vectors extracted over the full interval $t \in [0, 60]$ s and therefore represent the sustained sloshing behavior rather than an instantaneous pattern. The present approach, based on modal decomposition of the

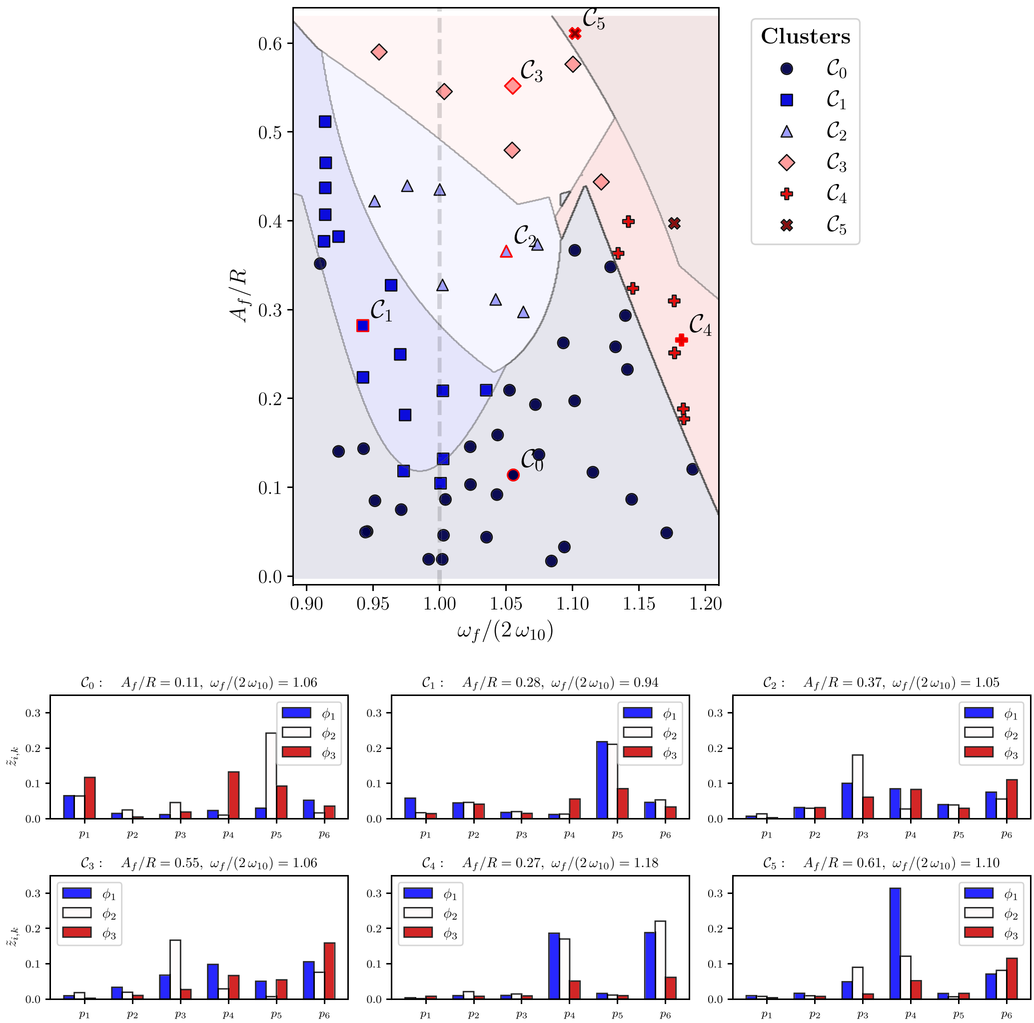

FIG. 10. Classification results for $H_l/D = 0.5$, with the data subdivided into six distinct clusters: $\{\mathcal{C}_0, \ldots, \mathcal{C}_5\}$, equaling the number of reference prototypes $p_j = p_6$ (see Sec. VI B). The experimental space was explored in $A_f/R \in [0.02, 0.62]$, with varying acceleration $A_f\omega_f^2/g \in [0.02, 0.77]$, while the dimensionless forcing frequency was investigated over the range of $\omega_f/(2\,\omega_{1,0}) \in [0.90, 1.20]$. The normalized energy signature of each cluster medoid, $\tilde{z}_{i,k}$ [see Eq. (17)], is shown in the bar plots. The bar amplitudes measure the similarity of the medoid to the different prototype-mode components ($\boldsymbol{\phi}_1$, $\boldsymbol{\phi}_2$, and $\boldsymbol{\phi}_3$), indicating which reference free-surface response dominates the cluster.

image sequences, circumvents the need for explicit interface reconstruction and allows the dominant dynamical features to be identified directly from the videos.

Cluster $\mathcal{C}_1$, centered at $A_f/R = 0.28$, $\omega_f/(2\,\omega_{1,0}) = 0.94$, captures points at moderately high forcing amplitudes $0.15 \leqslant A_f/R \leqslant 0.55$, yet mostly constrained to sub-resonant frequencies with $\omega_f/(2\,\omega_{1,0}) \leqslant 1.00$. The medoid energy signature shows that approximately 50% of the projected activation is associated with prototype p_5 [Fig. 8(b)]. This suggests that $\mathcal{C}_1$ is representative of a transitional regime, in which weak longitudinal dynamics emerge between nearly quiescent conditions and fully developed resonant motion, as also illustrated by the representative raw snapshot in Fig. 11.

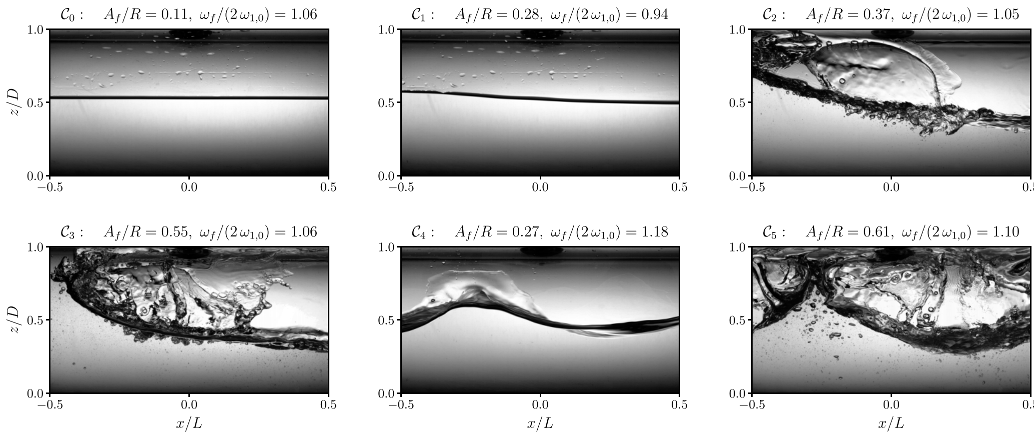

FIG. 11. Representative raw free-surface snapshots extracted from the six cluster medoids associated with the regime classification $\mathcal{C}_k$ shown in Fig. 10 for $H_l/D = 0.5$. The images provide a direct experimental visualization of the characteristic free-surface response associated with each cluster. All frames were selected during the developed stage of the motion, within the interval $t = 40 \pm 1$ s, and were chosen to emphasize dominant observable free-surface dynamics of each medoid within that window.

Cluster $\mathcal{C}_3$, with medoid at ($A_f/R = 0.55, \omega_f/(2\,\omega_{1,0}) = 1.06$), identifies high-amplitude forcing ($A_f/R \geqslant 0.45$) near resonance. Its energy signature is concentrated around prototype p_3, which is associated with wave-breaking of the fundamental longitudinal $m = 1$ mode [Fig. 7(c)], but also exhibits a nonnegligible contribution from p_6. This suggests that, for $\omega_f/(2\,\omega_{1,0}) \gtrsim 1.05$, the large-amplitude response is no longer purely described by the breaking $m = 1$ mode and possibly involves higher-order longitudinal content with the emergence of $m = 3$-type dynamics. In contrast, cluster $\mathcal{C}_2$ remains more clearly dominated by the wave-breaking longitudinal response associated with p_3. Thus, both $\mathcal{C}_2$ and $\mathcal{C}_3$ correspond to strongly nonlinear states near the principal instability region, but $\mathcal{C}_2$ may be interpreted as a predominantly pure wave-breaking $m = 1$ regime, whereas $\mathcal{C}_3$ marks the onset of a more complex high-amplitude state with possible higher-order longitudinal contributions.

Cluster $\mathcal{C}_0$ occupies the lower part of the forcing diagram and is primarily associated with weakly perturbed free-surface conditions below the onset of significant sloshing. Notably, $\boldsymbol{\phi}_3$ from p_4 contributes over 15%, while $\boldsymbol{\phi}_2$ and $\boldsymbol{\phi}_3$ from p_5 contribute over 30% of the total projected energy. These modes from prototype p_5 indicate a nearly quiescent free surface, which is also reflected in the representative raw snapshot shown in Fig. 11. Clearly, with over 30 samples identified, one can distinguish a strong boundary between stable free-surface dynamics [see Fig. 7(a)] and sloshing conditions (i.e., $\mathcal{C}_0$ vs. $\mathcal{C}_{\neg 0}$) located in the lower part of the diagram.

The histogram reveals that cluster $\mathcal{C}_4$ emerges from the interplay between prototypes p_4 and p_6. While p_4 represents pure longitudinal motion with $m = 3$, p_6 exhibits a mixed response involving both longitudinal ($m = 3$) and transverse ($n = 1$) modes. This suggests a distinct instability region at $\omega_f/(2\,\omega_{1,0}) \geqslant 1.20$. A detailed characterization of this regime, however, lies beyond the scope of this study.

Finally, for cluster $\mathcal{C}_5$, limited sampling in this high-amplitude and high-frequency region, together with the mechanical constraints of the sloshing table, resulted in only two data points. One of these corresponds to prototype p_4 at $A_f/R = 0.40$ and $\omega_f/(2\,\omega_{1,0}) = 1.17$, situated near the lower bound of this cluster.

Notably, within the isofrequency range $1.15 \leqslant \omega_f/(2\,\omega_{1,0}) \leqslant 1.20$, higher-order longitudinal motion becomes dominant, indicating a secondary instability region associated with the $m = 3$ mode. This behavior is consistent with nonlinear coupling between longitudinal, transverse, and oblique components, which can promote mixed-mode responses in horizontally oriented cylindrical tanks, where near-degenerate natural frequencies favor mode competition (see Fig. 17). The secondary harmonic branch associated with these modes develops near the primary subharmonic instability band of the longitudinal $m = 1$ mode, resulting in overlapping resonance tongues. As a result, the excitation frequency governs energy exchange between interacting modes, determining whether mixed or pure longitudinal responses prevail. This coupled-resonance behavior is consistent with the nonlinear Mathieu framework of El-Dib [34], which predicts the simultaneous occurrence of parametric instabilities and nested resonance regions. It also aligns with experimental observations of mode competition and mixed states in parametrically forced surface waves reported by Simonelli and Gollub [42] and more recently by Colville [50].

E. Parametric sloshing maps and fill level dependence

This subsection presents the final sloshing-regime maps for the tested fill ratios (see Table I). These maps are obtained through the iterative labeling strategy described in Sec. V C, in which the reference basis [see Eq. (14)] is progressively updated using cluster medoids until the convergence criteria of Sec. V C are met. This process improves cluster separation and reduces sensitivity to the initial hand-picked prototype set.

The sloshing intensity at each operating point is represented through the marker size computed as

$$I_i = \left(\sum_{r=1}^{n_R} \sigma_r^2 \right)^{1/2}, \quad n_R = 30. \tag{32}$$

Marker sizes follow the same linear mapping as in Sec. VI C. This quantity directly measures the fluctuation energy in the dominant sloshing structures, highlighting regions of strong activity.

Figure 12 shows the refined regime map for $H_l/D = 0.50$, building upon the initial clusters in Fig. 10(a). Uncertain near-boundary regions are indicated using the hatched rendering described in Sec. V D. Convergence was achieved after three iterations, with an ARI history {0.97, 0.99} [74]. The final medoids remained consistent with those from the first iteration, although convergence was triggered by the ARI threshold rather than the prototype-overlap condition. The low intra-cluster variance confirms the robustness of the final clusters and the distinct nature of the six regimes emerging from the prototype-guided clustering procedure (Figs. 7 and 8). The dominant spatial structure $\boldsymbol{\phi}_1$ of each medoid is shown in the surrounding panels, since it captures the leading large-scale free-surface motion and thus provides a concise representation of the main macro-dynamic features of each regime.

Cluster $\mathcal{C}_2$ occupies the central region of the map and corresponds to the pure longitudinal $m = 1$ mode. Its butterfly-like curvature, with slight doming near $x/L = \pm 0.5$, highlights the potential for interface breakup and liquid ejection near the tank heads. A similar pattern appears in clusters $\mathcal{C}_3$ and $\mathcal{C}_1$, reflecting a systematic increase in modal amplitude with forcing. At small forcing amplitudes, the system displays finite subharmonic responses characteristic of the weakly damped linear regime. As the forcing increases, the oscillations saturate due to nonlinear effects, and at the highest amplitudes ($A_f/R \gtrsim 0.45$), the motion becomes constrained by the tank geometry as the interface impinges on the bulkheads and cylindrical walls. In this high-forcing regime, vigorous mixing is induced through wave run-up, liquid ejection, and repeated wave breaking.

Clusters $\mathcal{C}_4$ and $\mathcal{C}_5$, appearing for $\omega_f/(2\,\omega_{1,0}) \geqslant 1.12$, exhibit higher-order longitudinal responses with $m = 3$, consistent with the prototype dynamics shown in Figs. 8(a) and 8(c). These regimes involve geometry-limited wave amplitudes and mixed-mode interactions, as discussed in Sec. VI D.

The maps in Fig. 12 also include the neutral stability boundaries predicted by the inviscid ($\zeta_{1,0} = 0$) and viscous ($\zeta_{1,0} = 0.004$) Mathieu-equation solutions of Sec. III. These boundaries are centered at the experimental value $2\,\omega_{1,0}$, partitioning stable and unstable (sloshing) regions.

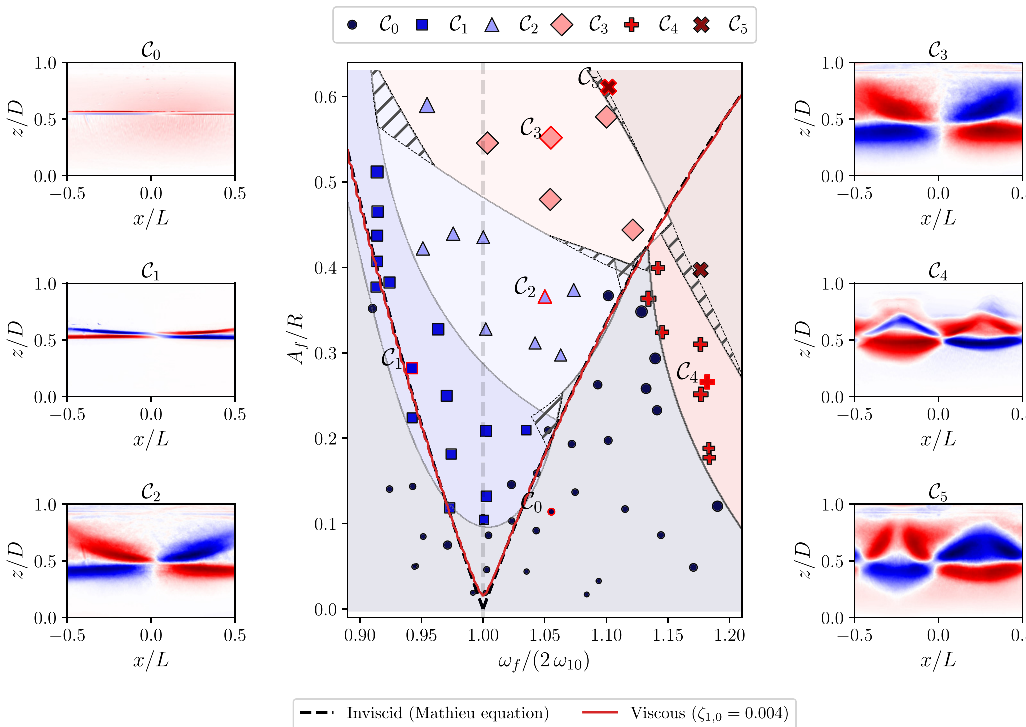

FIG. 12. Phase diagram of the dimensionless forcing amplitude, A_f/R, versus the frequency ratio, $\omega_f/(2\,\omega_{1,0})$, showing the stability boundaries in the vicinity of twice the fundamental sloshing eigenfrequency $\omega_{1,0}$ for a fill ratio of $H_l/D = 0.50$. Marker size highlights the sloshing-induced mixing intensity, I_i, quantified through the overall modal energy of the first thirty mPOD modes. Uncertain regions are indicated using the hatched rendering. For each cluster, the medoid's highest-energy spatial structure, $\boldsymbol{\phi}_1$, is displayed: $\mathcal{C}_0$, stable free-surface; $\mathcal{C}_1$, low-amplitude longitudinal motion; $\mathcal{C}_2$, longitudinal mode $m = 1$; $\mathcal{C}_3$, wave-breaking longitudinal mode $m = 1$; $\mathcal{C}_4$, mixed high-order dynamics; and $\mathcal{C}_5$, longitudinal mode $m = 3$. The spatial modes are shown using individual zero-centered symmetric diverging color scales, with limits set by the maximum absolute amplitude of each mode. Parametric-resonance predictions based on the Mathieu equation, in both the undamped ($\zeta_{1,0} = 0$) and damped ($\zeta_{1,0} = 0.004$) cases, are represented by the neutral-stability boundaries.

Classical results [26,29] show that viscous dissipation sets a critical excitation amplitude below which the free surface remains stable, in agreement with the present dataset. A marked increase in wave amplitude, captured here by cluster $\mathcal{C}_1$, occurs only for $A_f/R \gtrsim 0.1$ ($A_f \gtrsim 6.7$ mm). Overall, the predicted instability envelope aligns closely with the experimental classification, with most $\mathcal{C}_0$ (stable) points lying outside the Mathieu unstable region. The physics-informed framework therefore reinforces the consistency of the regime map, even though the Mathieu model—with only linear damping—slightly underpredicts the excitation amplitude required for instability.

Figure 13 presents the iteratively refined regime map for the fill ratio $H_l/D = 0.67 \pm 0.04$. Convergence was reached after six iterations, with an ARI history $\{0.64,\ 0.77,\ 0.93,\ 0.88,\ 1.00\}$. The experimental set contained $N_{\text{pts}} = 66$ points spanning $A_f/R \in [0.02, 0.58]$. Only five distinct regimes were identified, leading to a reduced prototype set ($n_P = 5$). The resulting clusters primarily capture stable free-surface dynamics ($\mathcal{C}_0$) and the fundamental longitudinal mode ($m = 1, n = 0$) excited near twice its natural frequency ($\omega_{1,0} \approx 7.12\,\text{rad s}^{-1}$).

The damping ratio for this fill level was estimated as $\zeta_{1,0} \approx 0.015 \pm 0.002$, representing an increase of 275% relative to $H_l/D = 0.50$. This confirms that damping increases for $H_l/D \geqslant 0.5$,

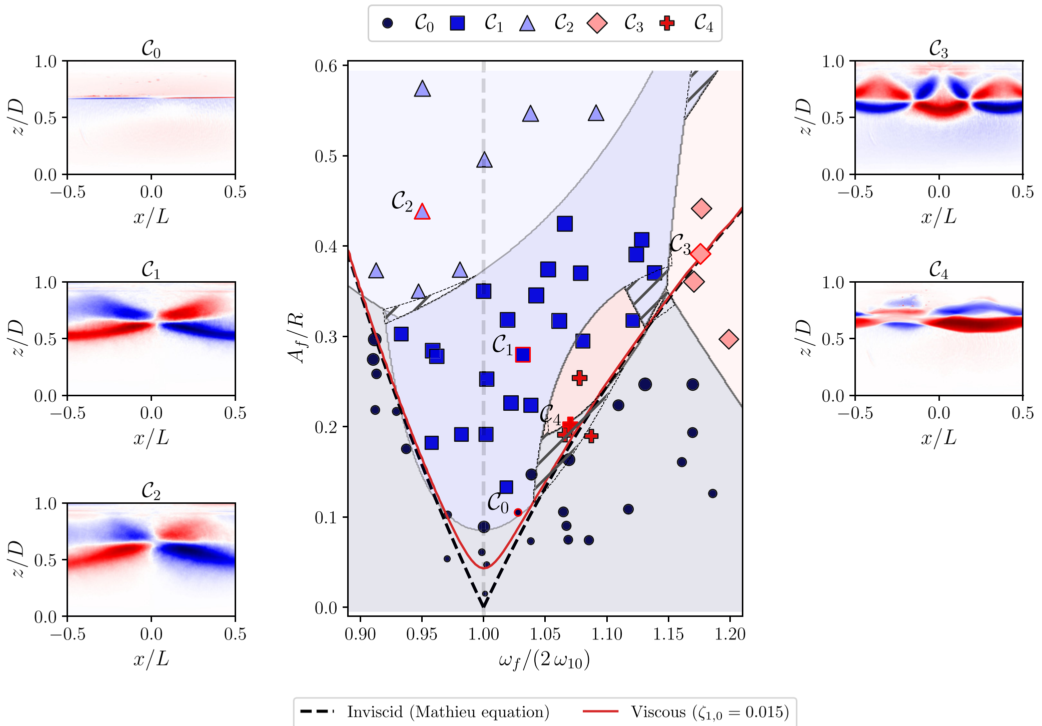

FIG. 13. Same as Fig. 12, but for a fill ratio of $H_l/D = 0.67$. Five sloshing regimes are identified: $\mathcal{C}_0$, stable free-surface response; $\mathcal{C}_1$, longitudinal ($m = 1$) sloshing; $\mathcal{C}_2$, breaking ($m = 1$) sloshing; $\mathcal{C}_3$, higher-order ($m = 4$) sloshing; and $\mathcal{C}_4$, mixed higher-order dynamics. The neutral-stability boundaries are overlaid to indicate the parametric-resonance region.

influenced by the dome cavities and curved sidewalls (Table I). This trend aligns with previous observations for spheroidal tanks, where damping exhibits a nonmonotonic dependence on fill level and reaches a minimum near the point of maximum interface area [64,78,80]. In contrast, canonical upright geometries (cylindrical or rectangular) typically show a leveling-off of the damping ratio beyond a critical fill height, allowing for fixed, dimensionless correlations based on the Galileo number [78,79]. The present findings therefore deviate from these classical trends, potentially indicating additional dissipation mechanisms induced by the complex wall curvature of horizontal tanks.

Clusters $\mathcal{C}_1$ and $\mathcal{C}_2$ capture two amplitude levels of the fundamental longitudinal mode. Points near the critical forcing fall in $\mathcal{C}_1$, displaying finite-amplitude oscillations with moderate wave heights. At high fill levels, the reduced ullage volume confines the free-surface motion and enhances interfacial exchange, leading to a rapid rise in mixing between $0.1 < A_f/R < 0.2$, after which saturation occurs, as indicated by the mixing metric I_i (marker size). Cluster $\mathcal{C}_2$ corresponds to strong wave-breaking at the domes with jet launches. Although these two regimes could be merged, they are kept distinct to capture the onset of breaking, which the mixing metric I_i alone does not fully reveal. This separation is important in nonisothermal applications where breaking drastically affects thermodynamic behavior, causing rapid pressure fluctuations or ullage collapse [12,81], and can enhance local evaporation when liquid impacts superheated walls [82].

A noteworthy transitional point appears at $A_f/R = 0.09$ and $\omega_f/(2\,\omega_{1,0}) = 1.00$, where the enlarged marker indicates elevated activity relative to surrounding $\mathcal{C}_0$ points. Its location near the cluster boundary reflects its borderline character. Conversely, the smallest-amplitude case in $\mathcal{C}_1$

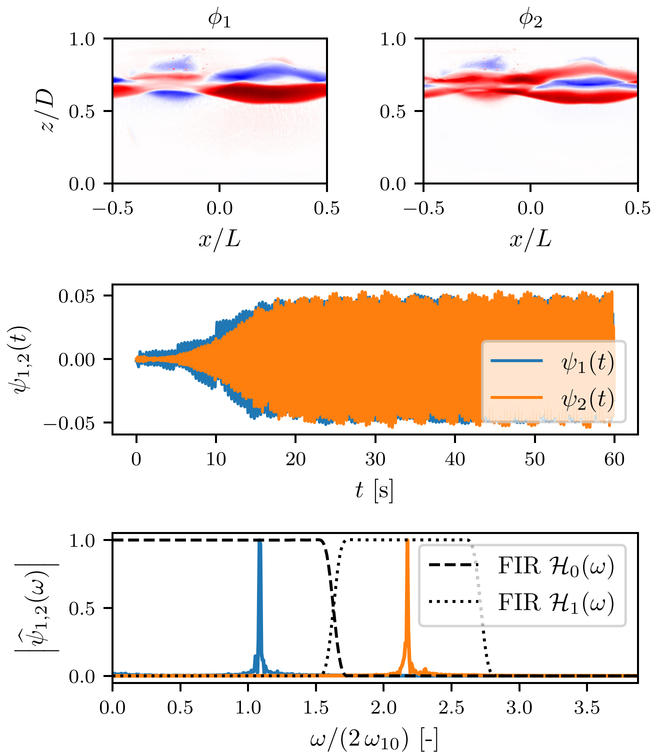

FIG. 14. mPOD modes $\boldsymbol{\phi}_{1,2}$, temporal coefficients $\boldsymbol{\psi}_{1,2}$, and spectra $|\hat{\boldsymbol{\psi}}_{1,2}|$ for $\mathcal{C}_4$ at $H_l/D = 0.67$ (see Fig. 13).

occurs at $A_f/R \approx 0.13$, slightly above the threshold for $H_l/D = 0.50$, suggesting that finer sampling would help resolve the transition.

Higher-order responses appear in clusters $\mathcal{C}_3$ and $\mathcal{C}_4$ (right panel of Fig. 13). Cluster $\mathcal{C}_3$ features a triple pulsating jet with five antinodes at $x/L = \pm 0.5, \pm 0.25$, and 0, corresponding to an $m = 4$-type pattern. This occurs at the map extremity under the same forcing conditions that activated the $m = 3$ mode at $H_l/D = 0.50$ (Fig. 12). The emergence of this $m = 4$ regime is consistent with the leveling of the corresponding natural frequency at high fill ratios (Sec. A, Fig. 17). Sparse sampling at high A_f/R for $\omega_f/(2\,\omega_{1,0}) \geqslant 1.15$, owing to acceleration limits of the shaking table, prevented us from fully capturing the transition between the $m = 4$ response in $\mathcal{C}_3$ and the longitudinal ($m = 1$) responses in $\mathcal{C}_1$, where time-modulated dynamics are expected.

Within $1.03 \leqslant \omega_f/(2\,\omega_{1,0}) \leqslant 1.13$, cluster $\mathcal{C}_4$ represents a transitional band between stable dynamics and the pure ($m = 1$) response. This region, delineated by dashed uncertainty contours, shows transverse motion with residual ($m = 3$) longitudinal content in the dominant spatial mode $\boldsymbol{\phi}_1$. To clarify the dynamics, Fig. 14 presents the temporal coefficients and spectra of the first two spatial modes (the third mode being dominated by noise). The medoid exhibits similarities to prototype p_6 [Fig. 8(c)], but without temporal modulation; instead, the system settles into a limit-cycle oscillation.

Finally, the weighting strategy in the physics-informed classifier (Sec. V D) proves effective: the resulting boundaries align closely with the inviscid Mathieu prediction, as points in clusters $\mathcal{C}_1$, $\mathcal{C}_2$, and $\mathcal{C}_4$ fall near the analytical instability envelope. This agreement is remarkable given the geometric complexity of the tank, although the Mathieu model with linear damping still slightly underpredicts the excitation level required for instability.

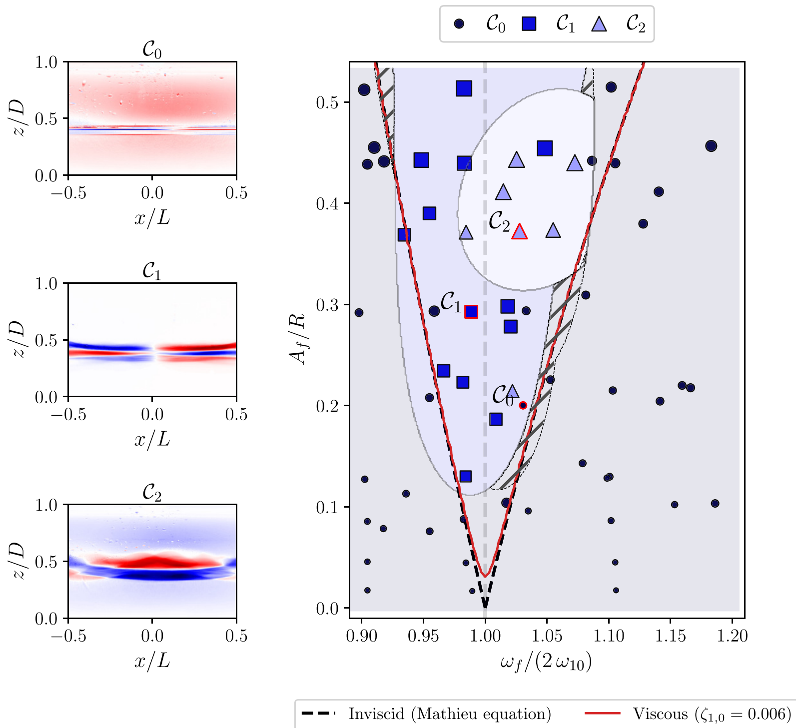

FIG. 15. Same as Fig. 12, but for $H_l/D = 0.40 \pm 0.04$, with the data subdivided into three clusters: $\mathcal{C}_0$, stable free-surface dynamics; $\mathcal{C}_1$, longitudinal mode $m = 1$; and $\mathcal{C}_2$, moderate-amplitude longitudinal motion. Parametric resonance, computed from the inviscid and viscous Mathieu equations, is shown through the corresponding neutral-stability boundaries.

Figure 15 shows the final regime map for $H_l/D = 0.40 \pm 0.04$, initialized using three prototypes ($n_P = 3,\ p_j = p_3$). Convergence was reached after five iterations, with an ARI history $\{0.67,\ 0.65,\ 0.96,\ 1.00\}$. Compared to the higher-fill cases, the range of observed dynamics is markedly reduced, with stable free-surface behavior ($\mathcal{C}_0$) dominating most of the parameter space. The narrowing of the instability region is evident, particularly when contrasted with the map at $H_l/D = 0.67$. This contraction results from the overall reduction in natural frequencies, experimentally determined as $\bar{\omega}_{1,0} \approx 5.32\,\mathrm{rad\,s^{-1}}$. The associated instability regions for higher modes also shrink and separate more distinctly in the forcing space, leading to weaker modal interactions. Consequently, higher-order responses—previously observed for $\omega_f/(2\,\omega_{1,0}) > 1.15$ at $H_l/D = 0.50$ and for $\omega_f/(2\,\omega_{1,0}) > 1.10$ at $H_l/D = 0.67$—do not arise within the explored range for this lower fill level.

The critical excitation amplitude appears near $A_f/R \geqslant 0.14$ ($A_f \geqslant 9.4\,\mathrm{mm}$), indicating that reduced liquid depth increases bottom-wall viscous dissipation and damping, thereby delaying the onset of parametric instability. This observation reinforces the need for a focused investigation into viscous dissipation mechanisms in horizontal geometries, as current literature offers limited insight into their influence in these conditions.

Cluster $\mathcal{C}_1$ captures the longitudinal response and occupies the Mathieu-unstable region. At this fill ratio, the camera provides a top-view observation of the interface, introducing nonnegligible three-dimensional effects that were minimal at $H_l/D = 0.50$ and $H_l/D = 0.67$. Cluster $\mathcal{C}_2$, appearing at larger forcing amplitudes ($A_f/R \geqslant 0.38$) and $1.00 \leqslant \omega_f/(2\,\omega_{1,0}) \leqslant 1.07$, displays pronounced sloshing absent from the other classes. Its dynamics resemble prototype p_5 [Fig. 8(b)],

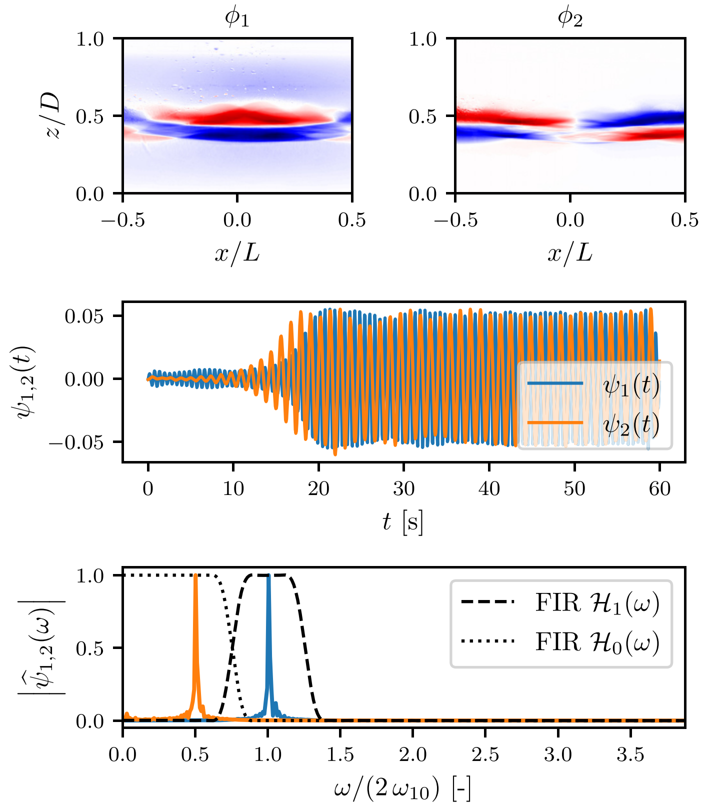

FIG. 16. mPOD modes $\boldsymbol{\phi}_{1,2}$, temporal coefficients $\boldsymbol{\psi}_{1,2}$, and spectra $|\hat{\boldsymbol{\psi}}_{1,2}|$ for $\mathcal{C}_2$ at $H_l/D = 0.40$ (see Fig. 15).

characterized by an $m = 2$ structure with a secondary $m = 1$ component, producing a mixed-mode longitudinal response. The corresponding medoid spatial modes, temporal coefficients, and spectra are shown in Fig. 16 for further clarification.

Overall, the regimes identified in Figs. 12–15 follow the classical behavior of parametrically excited (Faraday) waves. As shown by Benjamin and Ursell [29] and Brand and Nyborg [26], finite onset amplitudes arise from dissipation, while the ideal Mathieu model predicts infinitesimal excitation [1]. Consistent with these studies, the present maps exhibit the characteristic rounding of the instability tongues due to viscous and geometric effects [32,40].

However, across all three fill levels, the bottom portion of the region predicted unstable by the viscous Mathieu solution remains experimentally stable. Several factors may contribute to this discrepancy. One possibility is the presence of additional dissipation mechanisms under parametric forcing—such as amplitude-dependent viscous losses or weak nonlinear damping (with modal interaction) or contact-line hysteresis—not captured by the linear free-decay estimate. Yet, this explanation appears unlikely here, since the waves in this region have small amplitudes and therefore one might expect limited nonlinear content.

Another plausible explanation is that, within this band, the growth rate of the instability is extremely small, such that wave amplification does not become observable within the duration of the experiments. Nevertheless no appreciable growth trend was detected in the leading modal coefficients, indicating that—if an instability exists—its amplification is either too slow to emerge or effectively absent under the tested conditions. The discrepancy therefore likely reflects the combined effect of very slow (or null) parametric amplification and the simplified nature of the viscous Mathieu model, which does not capture subtle geometric or weakly nonlinear effects that may further stabilize the free surface near the stability threshold.

VII. CONCLUSIONS

This study experimentally investigated the dynamics of vertically driven sloshing in a horizontal cylindrical tank under gravity-dominated conditions. The primary objective was to construct a dimensionless sloshing regime map and identify the boundaries between distinct flow regimes near twice the first longitudinal natural frequency, $\omega_{1,0}$ - the principal zone of parametric instability. The results were expressed in nondimensional form using the relevant scaling laws.

Experiments were conducted at the von Kármán Institute's SHAKESPEARE facility using a horizontal cylindrical tank with spherical end caps and aspect ratio $L/R = 5.0$. Demineralized water was used as the working fluid, and liquid fill ratios in the range $H_l/D \in [0.40,\ 0.67]$ were explored over $A_f/R \in [0.02,\ 0.62]$, $A_f\omega_f^2/g \in [0.02,\ 0.94]$, and $\omega_f/(2\,\omega_{1,0}) \in [0.87,\ 1.20]$. This parameter sweep revealed a rich spectrum of interfacial behaviors near the primary resonance.

A data-driven methodology was introduced to construct semi-supervised regime maps by integrating unsupervised clustering and nonlinear classification within a reduced-order representation of the interface dynamics. The approach relies on a multiscale Proper Orthogonal Decomposition (mPOD) of stabilized high-speed image sequences to extract frequency-resolved modal features, which are then grouped into representative prototypes and classified using a physics-informed SVM. This framework provides a physically interpretable mapping of sloshing behavior linked directly to the Mathieu stability analysis.

Across the tested conditions, the system exhibited transitions from stable waves to pure and mixed longitudinal modes, with oscillation amplitudes ranging from weakly nonlinear to pronounced wave breaking. Experiments confirmed that a finite excitation threshold is required to reach these regimes, consistent with the viscous Mathieu formulation. However, the experimentally observed thresholds were significantly higher than those predicted by the viscous model. This underprediction likely arises from effects not captured by the linear damping inherent to the Mathieu equation, such as extremely slow subharmonic growth rates, weak nonlinear dissipation, and modal interactions. These mechanisms effectively raise the practical stability threshold, delaying—or suppressing—the onset of parametric amplification within the experimental time window.

At higher fill levels ($H_l/D = 0.50$ and 0.67), the dynamics became increasingly intricate due to competition between longitudinal modes. Mixed-mode responses emerged from the interaction between subharmonic and harmonic instability tongues associated with different sloshing modes, producing transitional regimes with amplitude modulation and intermittent switching. These behaviors are consistent with nonlinear coupling, in which energy is exchanged among near-resonant modes. The results indicate that, beyond the principal subharmonic resonance, higher-order mode interaction is a key factor governing sloshing behavior at elevated fill ratios. Within the explored parameter space, the resulting regime map captures the dominant and recurrent sloshing behaviors and provides a consistent organization of the observed flow responses. Regions associated with higher-order interactions and transitional dynamics remain only partially resolved in the present dataset, and future work could extend the analysis to additional natural frequencies and secondary resonance bands, further refining the boundaries of the identified regimes.

Overall, this study demonstrates a methodology for mapping sloshing regimes directly from high-speed image data through a combination of modal decomposition and data-driven classification. The resulting maps identify regions of stable behavior, large-amplitude longitudinal motion, and mixed-mode dynamics, providing a structured view of the flow response in the vicinity of the primary parametric resonance. The occurrence of wave breaking and mode interactions highlights conditions under which sloshing can significantly enhance mixing and alter the internal state of the fluid. The regime maps therefore provide a practical framework for anticipating the dominant sloshing response under given excitation conditions and for informing the design of active and passive sloshing-mitigation devices.

ACKNOWLEDGMENTS

This work has received financial support from various sources. The experimental setup, the experimental campaign, and G.C.A.C. were supported by the HASTA project (EU Horizon Europe, Grant Agreement No. 101138003). T.D.M. acknowledges support from the von Kármán Institute for Fluid Dynamics (VKI) through a fellowship awarded in the framework of his Research Master program. The postprocessing analysis was carried out through a joint effort between Francisco Monteiro, supported by a VLAIO grant from the Flemish Government (Reference HBC.2023.0897), and M.A.M., supported by the European Research Council under the European Union's Horizon Europe research and innovation programme (ERC Starting Grant RE-TWIST, Grant Agreement No. 101165479).

DATA AVAILABILITY

The data that support the findings of this study are available from the corresponding author upon request.

APPENDIX: ANALYTICAL SOLUTIONS FOR FUNDAMENTAL SLOSHING MODES IN HORIZONTAL CYLINDRICAL TANKS

A first-order approximation of the natural frequencies for sloshing modes (m, n) was obtained using the methodology of Hasheminejad and Soleimani [48]. This approach models the tank as a perfectly rigid, finite-length, horizontal cylinder with rigid end plates, partially filled to an arbitrary depth. The analysis assumes the fluid is inviscid, incompressible, and irrotational, so the velocity potential satisfies the Laplace equation. The dynamic and kinematic boundary conditions at the free surface are linearized. Separation of variables and application of Graf's translational addition theorem reduce the problem to an eigenvalue system for determining the natural frequencies.

Figure 17 presents the lowest set of modal frequencies for our tank with $R = 67.25$ mm and aspect ratio $L/R = 5.0$. These frequencies are determined by interpolating tabulated eigenvalues (Ω) between $L/R = 3.0$ and $L/R = 6.0$ at fill level ratios $H_l/D = 0.25$, $H_l/D = 0.50$, and $H_l/D = 0.75$.

Near twice the fundamental frequency $f_{1,0}$, higher-order branches converge. This convergence results in significant overlap across various fill ratios, increasing the likelihood of modal coupling.

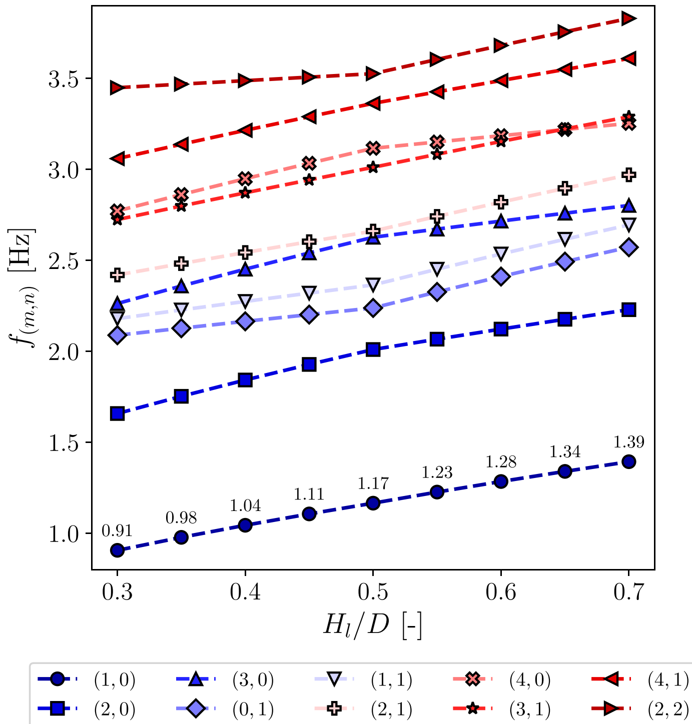

FIG. 17. Hasheminejad and Soleimani [48] derivation for the sloshing natural frequencies $f_{(m,n)}$ [Hz] as a function of the fill level H_l/D for a horizontal cylindrical tank with flat ends with $R = 67.25$ mm and aspect ratio $L/R = 5.0$. The curves are obtained by interpolation of the tabulated eigenvalues $\Omega = 4\pi^2 f_{m,n}^2 R/g$ in the fill coordinate $\bar{e} = 2H_l/D - 1$ and the aspect ratio L/R. Markers denote different modal families, while annotations are reported for the fundamental mode $(1,0)$.

[1] H. N. Abramson, *The Dynamic Behavior of Liquids in Moving Containers: With Applications to Space Vehicle Technology*, 1st ed. (Southwest Research Institute, San Antonio, TX, 1981).

[2] N. Kobayashi, T. Mieda, H. Shibata, and Y. Shinozaki, A study of the liquid slosh response in horizontal cylindrical tanks, J. Pressure Vessel Technol. **111**, 32 (1989).

[3] H. C. Mayer and R. Krechetnikov, Walking with coffee: Why does it spill? Phys. Rev. E **85**, 046117 (2012).

[4] F. T. Dodge, *The New "Dynamic Behavior of Liquids in Moving Containers,"* 1st ed. (Southwest Research Institute, San Antonio, TX, 2000).

[5] O. M. Faltinsen and A. N. Timokha, *Sloshing*, 1st ed. (Cambridge University Press, Cambridge, UK, 2009).

[6] R. A. Ibrahim, *Liquid Sloshing Dynamics: Theory and Applications*, 1st ed. (Cambridge University Press, Cambridge, UK, 2005).

[7] F. Monteiro, P. Marques, A. Simonini, L. Carbonnelle, and M. A. Mendez, Experimental characterization of non-isothermal sloshing in microgravity, Exp. Therm. Fluid Sci. **166**, 111473 (2025).

[8] A. V. Bazilevskii, V. A. Kalinichenko, and A. N. Rozhkov, Effect of fluid viscosity on the Faraday surface waves, Fluid Dyn. **53**, 750 (2018).

[9] T. Arndt, *Sloshing of Cryogenic Liquids in a Cylindrical Tank Under Normal Gravity Conditions*, 1st ed. (Cuvillier Verlag, Göttingen, 2012).

[10] A. van Foreest, *Modeling of Cryogenic Sloshing Including Heat and Mass Transfer*, 1st ed. (Cuvillier Verlag, Göttingen, 2014).

[11] P. Marques, S. Ahizi, and M. A. Mendez, Real-time data assimilation for the thermodynamic modeling of cryogenic storage tanks, Energy **302**, 131739 (2024).

[12] P. Marques, A. Simonini, L. Peveroni, and M. A. Mendez, Experimental analysis of heat and mass transfer in non-isothermal sloshing using a model-based inverse method, Appl. Therm. Eng. **231**, 120871 (2023).

[13] J. Miles, Resonantly forced surface waves in a circular cylinder, J. Fluid Mech. **149**, 15 (1984).

[14] A. Royon-lebeaud, E. J. Hopfinger, and A. Cartellier, Liquid sloshing and wave breaking in circular and square-base cylindrical containers, J. Fluid Mech. **577**, 467 (2007).

[15] E. J. Hopfinger and V. Baumbach, Liquid sloshing in cylindrical fuel tanks, Prog. Propul. Phys. **1**, 279 (2009).

[16] P. Guthrie, F. Gambioli, A. Chamos, S. Jones, J. Webb, J. Levenhagen, P. Behruzi, F. Mastroddi, A. Malan, S. Longshaw, A. Skillen, J. Cooper, L. Gonzalez, and S. Marrone, Sloshing wing dynamics—Project overview, in *Proceedings of the Transport Research Arena Conference* (Springer, Berlin, 2020).

[17] S. Marrone, A. Colagrossi, J. Calderon-Sanchez, and J. Martinez-Carrascal, Numerical study on the dissipation mechanisms in sloshing flows induced by violent and high-frequency accelerations. II. Comparison against experimental data, Phys. Rev. Fluids **6**, 114802 (2021).

[18] S. Marrone, A. Colagrossi, F. Gambioli, and L. González-Gutiérrez, Numerical study on the dissipation mechanisms in sloshing flows induced by violent and high-frequency accelerations. I. Theoretical formulation and numerical investigation, Phys. Rev. Fluids **6**, 114801 (2021).

[19] L. Constantin, J. De Courcy, B. Titurus, T. C. S. Rendall, and J. E. Cooper, Analysis of damping from vertical sloshing in a SDOF system, Mech. Syst. Sig. Process. **152**, 107452 (2021).

[20] L. Constantin, J. De Courcy, B. Titurus, T. C. S. Rendall, and J. E. Cooper, Nonlinear damping effects in vertically vibrating systems with violently sloshing liquid, J. Sound Vib. **544**, 117405 (2023).

[21] HASTA Project, Hasta project—The hydrogen aircraft sloshing tank advancement (2025), https://hasta-project.eu/, accessed: 2025-04-30.

[22] M. Faraday, On a peculiar class of acoustical figures; and on certain forms assumed by groups of particles upon vibrating elastic surfaces, Philos. Trans. R. Soc. London **121**, 299 (1831).

[23] J. W. S. L. Rayleigh, On the convection currents in a horizontal layer of fluid when the higher temperature is on the under side, Philos. Mag. **32**, 529 (1916).

[24] R. A. Ibrahim, Recent advances in physics of fluid parametric sloshing and related problems, J. Fluids Eng. **137**, 090801 (2015).

[25] F. T. Dodge, D. D. Kana, and H. N. Abramson, Liquid surface oscillations in longitudinally excited rigid cylindrical containers, AIAA J. **3**, 685 (1965).

[26] R. P. Brand and W. L. Nyborg, Parametrically excited surface waves, J. Acoust. Soc. Am. **37**, 509 (1965).

[27] L. Chang, Y. J. Jian, J. Su, R. Na, Q. S. Liu, and G. W. He, Nonlinear interfacial waves in a circular cylindrical container subjected to a vertical excitation, Wave Motion **51**, 804 (2014).

[28] L. Yu, M.-A. Xue, and Z. Jiang, Experimental investigation of parametric sloshing in a tank with vertical baffles, Ocean Eng. **213**, 107783 (2020).

[29] T. B. Benjamin and F. Ursell, The stability of the plane free surface of a liquid in vertical periodic motion, Proc. R. Soc. London A **225**, 505 (1954).

[30] J. Miles and D. Henderson, Parametrically forced surface waves, Annu. Rev. Fluid Mech. **22**, 143 (1990).

[31] J. Woodward, Fluid motion in a cylindrical tank of sector-annular cross section when subjected to a longitudinal excitation, Ph.D. Thesis, Georgia Institute of Technology, 1966.

[32] S. Ciliberto and J. P. Gollub, Chaotic mode competition in parametrically forced surface waves, J. Fluid Mech. **158**, 381 (1985).

[33] S. Ciliberto and J. P. Gollub, Pattern competition leads to chaos, Phys. Rev. Lett. **52**, 922 (1984).

[34] Y. O. El-Dib, Nonlinear Mathieu equation and coupled resonance mechanism, Chaos Solitons Fractals **12**, 705 (2001).

[35] J. B. Frandsen, Sloshing motions in excited tanks, J. Comput. Phys. **196**, 53 (2004).

[36] V. A. Kalinichenko, Breaking of Faraday waves and jet launch formation, Fluid Dyn. **44**, 577 (2009).

[37] L. Jiang, M. Perlin, and W. W. Schultz, Period tripling and energy dissipation of breaking standing waves, J. Fluid Mech. **369**, 273 (1998).
[38] H. Hashimoto and S. Sudo, Violent liquid sloshing in vertically excited cylindrical containers, Exp. Therm. Fluid Sci. **1**, 159 (1988).
[39] L. Kayal and R. Dasgupta, Jet from a very large, axisymmetric, surface-gravity wave, J. Fluid Mech. **975**, A22 (2023).
[40] S. Ciliberto and J. P. Gollub, Phenomenological model of chaotic mode competition in surface waves, Il Nuovo Cimento D **6**, 309 (1985).
[41] Z. C. Feng and P. R. Sethna, Symmetry-breaking bifurcations in resonant surface waves, J. Fluid Mech. **199**, 495 (1989).
[42] F. Simonelli and J. P. Gollub, Surface wave mode interactions: Effects of symmetry and degeneracy, J. Fluid Mech. **199**, 471 (1989).
[43] S. P. Das and E. J. Hopfinger, Parametrically forced gravity waves in a circular cylinder and finite-time singularity, J. Fluid Mech. **599**, 205 (2008).
[44] S. P. Das and E. J. Hopfinger, Mass transfer enhancement by gravity waves at a liquid–vapour interface, Int. J. Heat Mass Transf. **52**, 1400 (2009).
[45] H. Luo, W. Wu, B. Jiang, S. Guo, L. Huang, and B. Yue, Experiments and analysis of dynamic characteristics of liquid sloshing in horizontal Cassini tank, Phys. Scr. **98**, 075007 (2023).
[46] E. L. Grotle and V. Æsøy, Dynamic modelling of the thermal response enhanced by sloshing in marine LNG fuel tanks, Appl. Therm. Eng. **135**, 512 (2018).
[47] A. L. Martín López, Estudio teórico experimental de la estabilidad lateral en vehículos cisterna. Metodología para la determinación del umbral de vuelco, Ph.D. Thesis, Universidad Politécnica de Madrid, 2013.
[48] S. M. Hasheminejad and H. Soleimani, An analytical solution for free liquid sloshing in a finite-length horizontal cylindrical container filled to an arbitrary depth, Appl. Math. Modell. **48**, 338 (2017).
[49] Y. Han, X. Zhu, T. Li, W. Guo, and L. Pan, A semi-analytical study of the three-dimensional liquid sloshing in a horizontal cylindrical tank with an arbitrary liquid depth, Ocean Eng. **238**, 109722 (2021).
[50] S. W. Colville, Y.-M. Scolan, F. Gambioli, D. Greaves, E. Ransley, and Y. C. Lee, Faraday waves and period tripling in a horizontal circular tank, J. Fluid Mech. **1006**, A4 (2025).
[51] F. Saltari, M. Pizzoli, M. T. Migliorino, A. Binni, G. Coppotelli, F. Mastroddi, T. Pagliaroli, F. D. Duchetto, F. Gambioli, and R. Abarca, Experimental methodological investigations of sloshing-induced mass transfer coefficients for aircraft tanks, J. Thermophys. Heat Transfer **39**, 386 (2025).
[52] M. Pizzoli, F. Saltari, M. T. Migliorino, F. Mastroddi, and F. Gambioli, Modeling non-isothermal vertical sloshing via experimentally-driven Froude-dependent Nusselt number, Nonlinear Dyn. **114**, 443 (2026).
[53] T. Pagliaroli, F. Gambioli, F. Saltari, and J. Cooper, Proper orthogonal decomposition, dynamic mode decomposition, wavelet and cross wavelet analysis of a sloshing flow, J. Fluids Struct. **112**, 103603 (2022).
[54] D. Gligor, P. A. Marques, P. Salgado Sánchez, J. Porter, M. A. Méndez, and J. M. Ezquerro, Experiments on sloshing mitigation using tuned oscillating baffles, Phys. Fluids **36**, 092122 (2024).
[55] C. Chen, O. Li, D. Tao, A. Barnett, C. Rudin, and J. K. Su, This looks like that: Deep learning for interpretable image recognition, in *Advances in Neural Information Processing Systems 32 (NeurIPS 2019)*, edited by H. M. Wallach, H. Larochelle, A. Beygelzimer, F. d'Alché-Buc, E. Fox, and R. Garnett (Curran Associates, Inc., Red Hook, NY, 2019), pp. 8930–8941.
[56] P. Perner, Prototype-based classification, Appl. Intell. **28**, 238 (2008).
[57] M. Biehl, B. Hammer, and T. Villmann, Prototype-based models in machine learning, WIREs Cognit. Sci. **7**, 92 (2016).
[58] J.-W. Jang, A. Alaniz, L. Yang, J. Powers, and C. Hall, Mechanical slosh models for rocket-propelled spacecraft, in *Proceedings of the AIAA Guidance, Navigation and Control Conference* (American Institute of Aeronautics and Astronautics, Boston, MA, 2013).
[59] E. A. Cerda and E. L. Tirapegui, Faraday's instability in viscous fluid, J. Fluid Mech. **368**, 195 (1998).
[60] E. A. Cerda and E. L. Tirapegui, Faraday's instability for viscous fluids, Phys. Rev. Lett. **78**, 859 (1997).

[61] S. A. Ahizi, F. Monteiro, R. Abarca, and M. A. Mendez, Real-time identification of parametric sloshing-induced heat and mass transfer in a horizontally oriented cylindrical tank, Int. J. Heat Mass Transf. **264**, 128707 (2026).
[62] E. W. Lemmon, I. H. Bell, M. L. Huber, and M. O. McLinden, NIST standard reference database 23: Reference fluid thermodynamic and transport properties-REFPROP, version 10.0, National Institute of Standards and Technology (2018), https://www.nist.gov/srd/refprop.
[63] G. Bradski, The OpenCV library, Dr. Dobb's J. Software Tools **25**, 120 (2000).
[64] M. J. Casiano, *Extracting Damping Ratio from Dynamic Data and Numerical Solutions*, NASA Technical Memorandum NASA/TM–2016–218227 (NASA, Marshall Space Flight Center, Huntsville, AL, 2016).
[65] U. Tosun, R. Aghazadeh, C. Sert, and M. B. Özer, Tracking free surface and estimating sloshing force using image processing, Exp. Therm. Fluid Sci. **88**, 423 (2017).
[66] M.-R. Jiang, W.-J. Zhong, J.-X. Yu, P.-L. Liu, H.-J. Yin, S.-D. Wang, and Y.-X. Ma, Experimental study on sloshing characteristics in the elastic tank based on Morlet wavelet transform, China Ocean Eng. **32**, 400 (2018).
[67] J. Slavič, I. Simonovski, and M. Boltežar, Damping identification using a continuous wavelet transform: Application to real data, J. Sound Vib. **262**, 291 (2003).
[68] S. Hans, E. Ibraim, S. Pernot, C. Boutin, and C.-H. Lamarque, Damping identification in multi-degree-of-freedom system via a wavelet-logarithmic decrement—Part 2: Study of a civil engineering building, J. Sound Vib. **235**, 375 (2000).
[69] M. A. Mendez, M. T. Scelzo, and J.-M. Buchlin, Multiscale modal analysis of an oscillating impinging gas jet, Exp. Therm. Fluid Sci. **91**, 256 (2018).
[70] M. A. Mendez, D. Hess, B. B. Watz, and J.-M. Buchlin, Multiscale proper orthogonal decomposition (mPOD) of TR-PIV data—A case study on stationary and transient cylinder wake flows, Meas. Sci. Technol. **31**, 094014 (2020).
[71] R. Poletti, L. Schena, D. Ninni, and M. A. Mendez, Modulo: A Python toolbox for data-driven modal decomposition, J. Open Source Software **9**, 6753 (2024).
[72] M. A. Mendez, Generalized and multiscale modal analysis, in *Data-Driven Fluid Mechanics* (Cambridge University Press, Cambridge, UK, 2023) pp. 153–181.
[73] A. M. Ikotun, A. E. Ezugwu, L. Abualigah, B. Abuhaija, and J. Heming, K-means clustering algorithms: A comprehensive review, variants analysis, and advances in the era of big data, Inf. Sci. **622**, 178 (2023).
[74] W. M. Rand, Objective criteria for the evaluation of clustering methods, J. Am. Stat. Assoc. **66**, 846 (1971).
[75] C. Cortes and V. Vapnik, Support-vector networks, Mach. Learn. **20**, 273 (1995).
[76] K. Crammer and Y. Singer, On the algorithmic implementation of multiclass kernel-based vector machines, J. Mach. Learn. Res. **2**, 265 (2001).
[77] C.-W. Hsu and C.-J. Lin, A comparison of methods for multiclass support vector machines, IEEE Trans. Neural Networks **13**, 415 (2002).
[78] T. Arndt and M. Dreyer, Damping behavior of sloshing liquid in laterally excited cylindrical propellant vessels, J. Spacecr. Rockets **45**, 1085 (2008).
[79] H. N. Abramson, Space vehicle design criteria (structures): Slosh suppression, Tech. Rep. NASA SP-8031, NASA, Washington, D.C., 1969.
[80] H. Yang, R. Purandare, J. Peugeot, and J. West, Prediction of liquid slosh damping using a high resolution CFD tool, in *Proceedings of the 48th AIAA/ASME/SAE/ASEE Joint Propulsion Conference & Exhibit* (AIAA Aerospace Research Central, Reston, VA, 2012).
[81] P. Marques, S. Ahizi, F. Monteiro, B. Scheid, and M. Méndez, On the scaling of heat and mass transfer in cryogenic propellant tanks: A model-based and experimental analysis under static conditions and lateral sloshing, Appl. Therm. Eng. **279**, 127751 (2025).
[82] T. De Maria, F. Monteiro, S. Ahizi, G. C. A. Caridi, R. Abarca, and M. A. Mendez, Experimental analysis of sloshing-induced thermal mixing in horizontally oriented cylindrical tanks subjected to vertical acceleration, in *Proceedings of the 11th European Conference for Aeronautics and Aerospace Sciences* (EUCASS Association, Rome, Italy, 2025).